

# The fate of nitrogen in deep magma oceans

Ekanshu Mallick<sup>a,\*</sup>, Kelsey Prissel<sup>b</sup>, Kevin Righter<sup>c</sup>, Colin R.M. Jackson<sup>a</sup>

<sup>a</sup> Department of Earth and Environmental Sciences, Tulane University, United States

<sup>b</sup> Department of Earth, Atmospheric and Planetary Sciences, Purdue University, United States

<sup>c</sup> Department of Earth and Environmental Sciences, University of Rochester, United States

## ARTICLE INFO

Associate Editor: Fabrice Gaillard

### Keywords:

Nitrogen  
Metal-silicate partitioning  
Core Formation  
Magma Ocean  
Volatiles  
LH-DAC

## ABSTRACT

Nitrogen is important in planetary evolution because it is essential to life and the most abundant element in Earth's atmosphere. Here, we investigate how core formation affects the distribution of N within accreting terrestrial planets. We conducted laser-heated diamond anvil cell experiments (LH-DAC) over a wide range of high pressure–temperature–compositional (PTX) conditions (38–103 GPa, 2728–5609 K,  $-1.95$  to  $-1.03$   $\Delta$ IW, 0.5–3.7 NBO/T) to study nitrogen partitioning in metal-silicate systems. Combining our data with existing low and high PT results, we developed a nitrogen partitioning model applicable from early accretion to extreme PT stages associated with giant impacts. We test the robustness of our model by accurately predicting nitrogen partitioning in a multi-anvil experiment conducted independently at 15 GPa, 2573 K with oxygen fugacity of  $-2.5$   $\Delta$ IW. Our model shows that increasing pressure, oxygen fugacity, and N concentration in the alloy make nitrogen more siderophile, while increasing temperature, oxygen and silicon contents in the alloy, and the SiO<sub>2</sub> content of the silicate melt make nitrogen less siderophile. Application of our model to core formation conditions under oxidized and reduced scenarios suggest that nitrogen can be siderophile or lithophile under low PT conditions but exhibits a neutral partitioning at high PT conditions ( $> 100$  GPa, 5000 K) over a wide range of bulk planet compositions. Using our model, along with partitioning models for S and C, we examine how core formation scenarios can fractionate C/N and S/N ratios in the BSE. Our model suggests that backreaction of volatile rich cores from reduced, smaller impactors (sub-Mars-sized) within deep magma oceans can impart a wide range of C/N and S/N ratios on the magma ocean. We find that the amount of silicate entrainment has a strong control on elemental fractionations imparted to the magma oceans. Elevated C/N and S/N ratios are associated with larger degrees of silicate entrainment, and vice versa. Thus, Earth's apparent depletion of N may relate to its volatiles being reprocessed within deep magma oceans, possibly during the end stages of accretion.

## 1. Introduction

Nitrogen, being the most abundant element in the atmosphere, plays a pivotal role in Earth's life-forming processes and is paramount in sustaining habitability on the planet. Understanding the distribution and abundance of nitrogen within the planet involves delving into its accretionary history, where planetary-scale processes like core formation and atmospheric evolution have influenced the planet's chemistry. As a volatile siderophile element (VSE), the geochemical behavior of nitrogen strongly impacts its distribution during these accretionary stages.

Earth accumulated its mass through numerous impacts that generated global or partial magma ocean (MO) environments (Elkins-Tanton, 2012; Tonks and Melosh, 1993; Wetherill, 1985). These MO

environments facilitate reactions that set the abundance and distribution of different elements, including nitrogen within the planet (Hirschmann, 2016; Suer et al., 2023). Magma ocean production in early accretionary stages may have been facilitated by radiogenic heating (LaTourrette and Wasserburg, 1998; Lee et al., 1976; Urey, 1956), but later stages of magma ocean production were likely driven by impacts from differentiated planetary bodies (Halliday et al., 2001; Tonks and Melosh, 1993; Wetherill, 1980). Towards the terminal stages of its accretion, production of global and deep magma oceans were driven by giant impacts, with pressures exceeding 100 GPa and temperatures over 6000 K (Canup and Asphaug, 2001; Tonks and Melosh, 1993), and redistribute elements within global planetary reservoirs.

Magma oceans are instrumental in creating compositional differentiation across the different accretionary stages, from planetesimals to

\* Corresponding author at: Tulane University, 101 Blessey Hall, New Orleans, LA 70118, United States.

E-mail address: [emallick@tulane.edu](mailto:emallick@tulane.edu) (E. Mallick).

<https://doi.org/10.1016/j.gca.2025.02.020>

Received 11 September 2024; Accepted 18 February 2025

Available online 5 March 2025

0016-7037/© 2025 The Author(s). Published by Elsevier Ltd. This is an open access article under the CC BY license (<http://creativecommons.org/licenses/by/4.0/>).

protoplanets (Davies, 1985; Halliday et al., 2001; Lee et al., 1976; Tonks and Melosh, 1993; Urey, 1956). During impacts that produce MO environments in protoplanets, the disrupted cores of differentiated impactors smear through the MO before eventually merging with the proto-core (e.g. Dahl and Stevenson, 2010). Fluid dynamic studies show that the disrupted core emulsifies to different degrees and descends through the magma ocean while entraining different amounts of silicate mass from the magma ocean (e.g. Deguen et al., 2014). This allows for continuous backreaction of the disrupted core with the entrained silicate mass of the larger body which can redistribute elements between the MO and the reacting metal based on their relative siderophilicities. Additionally, the MO interacts with the evolving atmosphere, which terrestrial planets like Earth could acquire during their accretion. This MO-atmosphere interaction allows for the redistribution of elements between these two reservoirs based on their volatile natures, influenced by processes like magma ocean degassing and atmospheric loss, hydrodynamic outflow, non-thermal loss due to a weak or non-existent magnetosphere, and giant impact driven loss (Genda and Abe, 2003; Lammer et al., 2008; Moynier et al., 2012; Schlichting et al., 2015; Sekiya et al., 1980; Tucker and Mukhopadhyay, 2014). Consequently, the VSE behavior of nitrogen makes its abundance and distribution within a terrestrial planet susceptible to both core-MO and MO-atmosphere interactions.

Observations on the distribution of nitrogen compared to other VSEs (H, C, S) indicate that N is highly depleted relative to H, C, and S, in the bulk silicate Earth (BSE) reservoir when normalized to CI chondrites (Halliday, 2013; Marty, 2012). This depletion could result from core formation, volatile loss associated with atmospheric evolution or early solar system processes (e.g. Bergin et al., 2015). Although, other studies also suggest that the mantle has enough capacity to host N and that the previously observed depleted N signature in BSE may not accurately account for the N sequestered in the lower mantle, which when accounted for may not suggest an apparent depletion of N (Johnson and Goldblatt, 2015; Yoshioka et al., 2018). The depletion of N within BSE, the exact nature of the VSEs source, the mechanisms involved and the timing of VSE delivery to the planet remain debated topics (e.g. Albarède, 2009; Alexander, 2022; Braukmüller et al., 2019; Grewal et al., 2024; Hirschmann, 2016; Holzheid et al., 2000; Marty, 2012; Newcombe et al., 2023; Wang and Becker, 2013). Regardless of these uncertainties, the partitioning of N in MO-core interactions and the associated backreactions is key to understanding how N gets distributed in both the smaller differentiated impactors that likely delivered volatiles as well as in large terrestrial planets like Earth, which experienced core formation up to extreme PT conditions associated with the later giant impact stages.

In this context, there has been significant work towards understanding how nitrogen behaves in metal (core) – silicate (magma ocean) systems that offer insight on the siderophilicity of nitrogen, particularly at lower PT conditions, typically below 20 GPa (Dalou et al., 2017, 2019a; Grewal et al., 2019a, 2019b, 2021a, 2022b; Jackson et al., 2021; Kadik et al., 2011, 2013; Li et al., 2023, 2016; Roskosz et al., 2013; Shi et al., 2022; Speelmanns et al., 2019). Beyond this pressure range, data are sparse and are primarily derived from two studies using laser heated diamond anvil cells (LH-DAC) to investigate metal-silicate reactions (Huang et al., 2024; Jackson et al., 2021). While these LH-DAC data provide insights into the behavior of nitrogen under high PT conditions, they struggle to independently constrain the effects of pressure–temperature–compositional (PTX) parameters. The inherent covariance of PTX parameters in LH-DAC experiments complicates the interpretation of nitrogen partitioning between metal and silicate. To address this, more independent datasets from LH-DAC experiments covering non-overlapping PTX domains are necessary. Such datasets can help confirm the consistency of PTX parameter effects or isolate the impact of each parameter, thereby improving the accuracy of nitrogen behavior predictions under high and extreme core formation conditions.

Without the ability to confidently predict the siderophilicity of

nitrogen over the full range of pressures, temperatures, and compositions that prevailed during core formation, we cannot know how Earth's accretionary period set the abundance of nitrogen in the mantle which was eventually available to support habitability. Towards this end, we ran high PT multi-anvil (MA) and laser heated diamond anvil cell (LH-DAC) experiments to better constrain nitrogen's partitioning during the extreme conditions of core formation. We ran experiments between 15 GPa and 103 GPa with temperatures up to 5609 K and oxygen fugacity ranging between  $-2.5$  to  $-1$   $\Delta$ IW to determine the effects of pressure, temperature, oxidation state, and composition on nitrogen's partitioning. We conclude by applying our data to predict VSE fractionations in deep magma oceans.

## 2. Methods

We designed a series of laser heated diamond anvil cell (LH-DAC) experiments to test the effect of pressure, temperature, silicate and alloy melt composition, and oxygen fugacity of the system on nitrogen partitioning between metal-silicate ( $D_N^{\text{m/s}}$ ) (Table 1). Additionally, we ran a multi-anvil (MA) experiment at 15 GPa to test the efficacy of our nitrogen partitioning model based on previously reported high pressure LH-DAC experiments ( $>20$  GPa), low pressure piston cylinder, MA experiments ( $<20$  GPa) and our new experiments. The different experimental setups and their compositional designs are discussed below.

### 2.1. Starting compositions

We utilize a variety of starting compositions to explore the effect of composition (X) on the partitioning of nitrogen. Our nominal silicate composition is adapted from the primitive MORB chemistry from Hirschmann et al. (1998) (62a, Appendix A). We modify their composition to a relatively high Mg# (0.83 compared to 0.77) and no alkali elements. We make these modifications to enable exploration of compositional effects around a relatively undifferentiated mantle composition (e.g. Green and Ringwood, 1963). The mixture (SAMCF in Fig. 2.1) was prepared by mixing oxides of  $\text{SiO}_2$ ,  $\text{Al}_2\text{O}_3$ ,  $\text{FeO}$ , and  $\text{MgO}$ .  $\text{FeO}$  was prepared from  $\text{Fe}_2\text{O}_3$  by reducing it in a gas mixing furnace at 1373 K under  $\text{CO-CO}_2$  oxygen fugacity ( $f_{\text{O}_2}$ ) for 45 min. An alumina crucible was used for doing this reduction. This was done to ensure that Fe added to the bulk composition is dominantly divalent.  $\text{CaO}$  was added after decarbonating  $\text{CaCO}_3$  at  $\sim 1073$  K for 2–3 h. The mixture was homogenized using mortar and pestle, and ball-milled in an alumina crucible for 30 min. Ball-milling led to additional alumina getting added to our starting composition. This contamination was up to 5 wt% as measured using energy dispersive spectroscopic (EDS) in an alumina free starting composition that was ball-milled for 30 min. We accounted for this contamination when making our starting mixture, although the contamination does lead to variations in the alumina content of our experimental melts (discussed later).

Post ball-milling, 25–30 mg of the mixture was then melted in a gas mixing furnace at 1600 K on a rhenium wire loop and at  $f_{\text{O}_2}$  equivalent of QFM for 30 min. The  $f_{\text{O}_2}$  ensured a dominant divalent Fe in the melt to facilitate later equilibration with Fe alloy (O'Neill, 1987). Although it is possible that there may be some  $\text{Fe}^{3+}$  in the melted glass since  $f_{\text{O}_2}$  of QFM at 1600 K is indeed close to that of WH (Campbell et al., 2009; Fudali, 1965). The melted (glass) bead was then embedded in epoxy and evaluated for homogeneity. We used a Hitachi S-3400 SEM and EDS analysis to evaluate and validate the homogeneity of synthesized silicate glass and the absence of quench crystals. Additionally, we created silicate compositions for our  $f_{\text{O}_2}$  series of experiments (Table 1) by modifying the nominal silicate composition with variable  $\text{FeO}$  contents (1 and 4 wt%). Finally, we used iron nitride for our metallic-alloy composition, and source of N (7.47 wt% nitrogen, Alfa Aesar), in all our experiments.

**Table 1**

**Experimental conditions.** The Glass:Fe<sub>x</sub>N:Glass sample design represents our nominal compositional design used for the pressure series and the MgO:2Silicate + 1Fe<sub>x</sub>N:MgO design represents our MgO saturated compositional design. The N-MA-15–1 experiment is the multi-anvil experiment.

Experiment	Sample Design	P (GPa)	±	T (K)	±	ΔIW	±	log D <sub>N</sub> <sup>m/s</sup> (at)	±
N28-3	Glass:Fe <sub>x</sub> N:Glass	38	7	2728	68	−1.91	0.03	1.03	0.13
N32-2	Glass:Fe <sub>x</sub> N:Glass	40	1	3395	79	−1.49	0.1	0.50	0.08
N49-1	Glass:Fe <sub>x</sub> N:Glass	63	2	4774	61	−1.57	0.11	0.40	0.05
N65-3	Glass:Fe <sub>x</sub> N:Glass	83	2	5171	60	−1.73	0.06	0.26	0.04
N39-1	Glass:Fe <sub>x</sub> N:Glass	52	3	4316	42	−1.87	0.01	0.40	0.13
N39-2	Glass:Fe <sub>x</sub> N:Glass	53	3	4845	73	−1.36	0.08	0.40	0.12
*NFO_2-2Fe-1	Glass:Fe <sub>x</sub> N:Glass	69	4	5038	22	−1.42	0.03	0.33	0.07
*NFO_2-2Fe-2	Glass:Fe <sub>x</sub> N:Glass	65	4	3434	187	−1.95	0.03	0.40	0.05
*NFO_2-4Fe-1	Glass:Fe <sub>x</sub> N:Glass	67	2	5120	163	−1.68	0.15	0.31	0.09
**NMO50-3	MgO:2Silicate + 1FeN:MgO	68	1	5275	61	−1.24	0.06	0.61	0.11
**NMO30-2	MgO:2Silicate + 1FeN:MgO	43	1	4066	420	−1.03	0.02	1.00	0.06
N75-1	Glass:Fe <sub>x</sub> N:Glass	86	2	5365	295	−1.42	0.04	0.28	0.01
N85-3	Glass:Fe <sub>x</sub> N:Glass	103	2	5609	202	−1.15	0.07	0.23	0.04
*NFO_2-1Fe-1	Glass:Fe <sub>x</sub> N:Glass	60	2	4937	460	−1.63	0.1	0.22	0.03
*NFO_2-1Fe-2	Glass:Fe <sub>x</sub> N:Glass	60	2	4868	93	−1.54	0.02	0.31	0.02
**NMO50-1	MgO:2Silicate + 1FeN:MgO	67	1	4717	140	−1.05	0.02	0.79	0.06
N-MA-15–1	2Glass + 1FeN	15	0.5	2773	20	−2.51	0.06	1.19	0.21

Reported pressure was measured using diamond edge Raman spectroscopy and represents the average pressure in the sample chamber after heating and includes thermal pressure. Pressure uncertainties are the standard deviation of pressure measurements across the sample chamber. The temperature measurements are average values of multiple spectra collected in succession with reported uncertainties as their standard deviation. ΔIW was calculated using methods in section 3.3. Error on ΔIW was computed by propagating analytical uncertainties for FeO and Fe. D<sub>N</sub><sup>m/s</sup> is the partition coefficient of nitrogen calculated from analytical measurements in mole fraction. Error on D<sub>N</sub><sup>m/s</sup> were calculated by propagating analytical uncertainties for N in the silicate and the metal. Experiments designed with variable FeO content in starting composition to explore the effect of oxygen fugacity. (\*\*) MgO-saturated DAC experiments.

## 2.2. Laser heated diamond anvil cell experiments

After preparing our starting compositions, we assembled the diamond anvil cells (DAC) at Tulane University. Fig. 1a shows a schematic cross section of the symmetric DAC assembly with a loaded sample (silicate-alloy). We used diamond culet diameters between 200–400 μm to compress our samples over the span of our targeted high pressures. The seats holding the diamonds were made of tungsten carbide on both the piston and cylinder sides. The gasket was prepared by pre-indenting a rhenium (Re) foil to ~ 25–30 μm. The desired thickness was created by tracking ruby fluorescence during compression (Mao et al., 2008; Shen et al., 2020). We then created the sample chamber by using a micro-laser cutter to drill a cylinder into the pre-indented Re foil such that it aligns centrally with the axes of the diamonds. The fractional diameter of the sample chamber was between 0.33–0.66 of the culet diameters, with the choice depending on the experimental pressure.

The starting materials were then prepared to be loaded into the sample chamber. Preparations involved making discs of starting materials (silicate glass, metallic alloy, MgO powder, silicate + metallic alloy

mix) which were then stacked into the sample chamber depending on the stack design (Fig. 2). To make the silicate discs, we embedded our silicate glass into epoxy and polished it to a thickness of ~ 10–15 μm. This thin layer of silicate glass was then laser cut to match the diameter of our sample chamber. For the metallic alloy discs, we compressed iron nitride powder using a diamond anvil to ~ 7–10 μm thickness, and laser cut alloy discs to match the sample chamber diameter. Additionally, MgO discs and discs of the silicate + metallic alloy mix were prepared for our MgO-saturated experiments and are described below. The laser cut discs were then loaded into the sample chambers guided by different designs as explained below.

## 2.3. Layer designs for experiments

The layer designs in our sample chambers were adapted from our previous LH-DAC studies (Jackson et al., 2021, 2018). We planned two different designs for our experiments, a nominal design (silicate glass-metallic alloy-silicate glass) that was used for the pressure series and a MgO-(silicate + metallic alloy mix)-MgO design (MgO-saturated

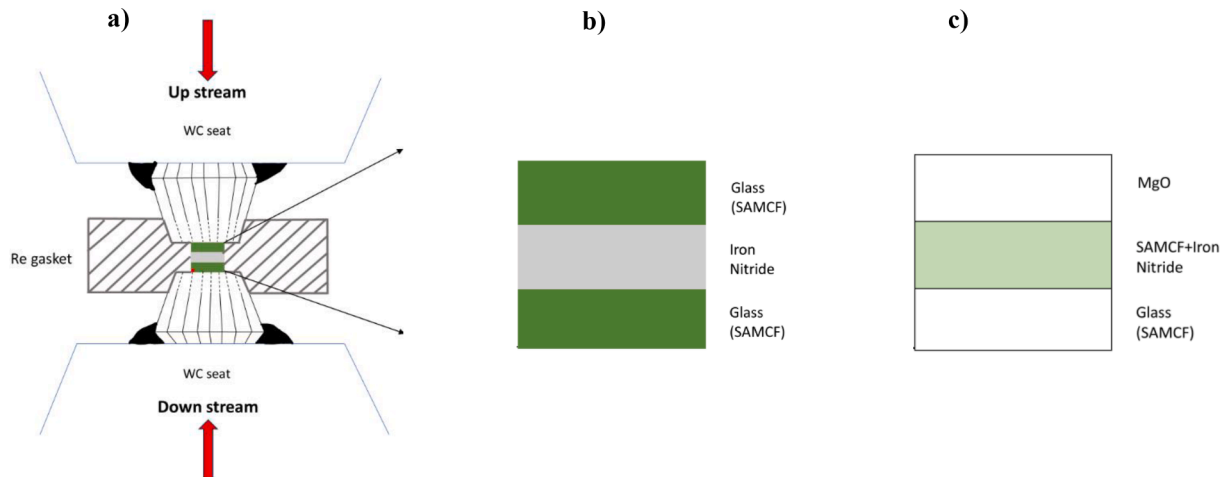


**Fig. 1.** (a) Schematic of an assembled diamond anvil cell. Red arrows: IR laser beam direction. Layered stacking of starting compositions for (b) Nominal design, (c) MgO saturated design. SAMCF depicts the components SiO<sub>2</sub>, Al<sub>2</sub>O<sub>3</sub>, MgO, CaO, and FeO in the glass/silicate starting composition.

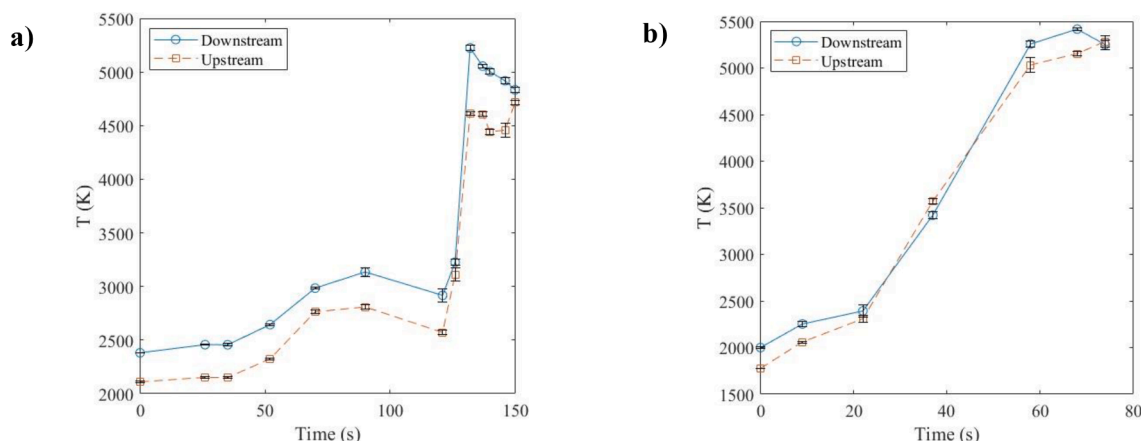


**Fig. 2.** Time-Temperature paths of experiments (a) N49-1 and (b) NMO50-3. The upstream and downstream temperatures were monitored throughout the run duration of the experiment. Error bars are standard deviations on the number of T-measurements acquired at each time increment (x-axis) from the beginning of laser heating the sample marked at 0 s.

experiments) that was run to test the effect of melt composition on  $D_N^{m/s}$  (Fig. 1b, c). The nominal layer design for our DAC experiments has an iron nitride disc sandwiched between silicate glass discs (Fig. 1b). The glass discs provided thermal and chemical insulation of the metal from the diamonds. Besides running our pressure series using this design, we also ran a few experiments with different glass compositions (variable FeO composition) to explore variations in oxygen fugacity of the system (see Table 1 and results). For the MgO-(silicate + alloy)-MgO designs (Fig. 1c), we mixed the silicate and the metallic alloy powders in a 2:1 ratio (wt%) and made discs of 10–15  $\mu\text{m}$  thickness. A disc of this mixture is sandwiched between discs of MgO that were prepared by compression to 10–15  $\mu\text{m}$  thickness and were laser cut as well. Often the laser cut MgO discs were not coherent, and their shapes needed modification using a tungsten needle to fit the sample diameter.

To explore the effect of nitrogen concentration on the partitioning of nitrogen, we modified the alloy by mixing different proportions of iron nitride and Fe powders. However, such mixtures suffered from a lack of uniform grain size distribution when mixed using the alumina ball-mill and had larger Fe grains that resulted in inefficient heating and failure during experimentation. This prevented us from systematically evaluating the effect of nitrogen concentration on its partitioning in our experiments.

The assembled DACs were heated in a vacuum oven at 393 K for 12–24 h to remove moisture absorbed by hygroscopic components in the sample chamber. The DACs were then sealed off from moisture by compressing them to  $\sim 2$ –5 GPa.

#### 2.4. Laser heating

The assembled and sealed off DACs were laser heated at GSECARS (13-ID-D beamline, Advanced Photon Source, Argonne National Lab) to react N-bearing metal and silicate under PT conditions highlighted in Table 1. Specific target pressures were reached and monitored using diamond edge Raman measurements (Akahama and Kawamura, 2006; Dobrosavljevic et al., 2023). We recorded the average pressure of the sample chamber and the associated standard deviation after each heating cycle using diamond edge. Additionally, during each heating cycle, we used the XRD measurements of mineral phases (e.g., Fe, MgO) with known equations of state to estimate pressure (Fig. S3) (Ono et al., 2010; Sha and Cohen, 2010; Wu et al., 2008). Integration of XRD images and visualization was done using the software DIOPTAS (Prescher and Prakupenka, 2015). We acknowledge that during heating, MgO or Fe reacting in the hotspot may not be pure phases and hence using EOS for pure MgO or Fe to determine pressure might not be reliable. However, among the multiple MgO diffraction peaks, the peaks corresponding to

the lowest d-spacing likely represent unreacted MgO around the spot being heated. Since most samples in our experimental design were not MgO saturated, we could not avoid sampling contaminated MgO to get reliable pressure estimates. Instead, we rely on diamond edge to determine the final pressures for all our samples post quenching (Table 1). Where unreacted MgO is sampled by the X-ray beam (few MgO saturated designs), there is some similarity in the pressure measured using diamond edge and that measured from diffraction peaks of unreacted MgO (Fig. S3). Using diamond edge, the pressures determined pre-heating are usually up to 5 GPa lower than the pressure measurements post quench.

We used a focused  $\sim 15$ –20  $\mu\text{m}$  IR laser beam ( $\lambda = 1,064$  nm) to heat our samples, coupled from both upstream and downstream sides of the DAC. We first annealed each experiment at  $\sim 1500$ –1800 K to lower any existing pressure gradients within the sample chamber and to identify regions that coupled well with the laser. Selected regions were then heated in a new heating cycle. To heat, we manually controlled the power ramp on the upstream (US) and the downstream (DS) side steadily up to  $\sim 2000$  K while maintaining minimal temperature difference between the two sides. Around 2000 K, we rapidly increased power input until melting was achieved. Melting was confirmed by the disappearance of diffraction peaks of any solid phase (Fe-hcp,  $\text{MgSiO}_3$ ) and an increase in diffuse scattering, collected via in-situ XRD measurements during laser heating. Melting was also visually confirmed by a sudden increase in the incandescence of the samples. Some experiments displayed flickering incandescence at higher powers. Many hotspots that displayed flickering later had uncontrolled temperature drops and associated heating failures. Such experiments were not included in our dataset. After confirmation of melting, we acquired repeat measurements of the temperature to confirm temperature stability during the molten state of the heating-spot along with their corresponding XRD measurements. Finally, the sample was quenched by cutting off laser power. The high conductivity of diamond was instrumental for rapid heat loss and quenching. Each heating cycle typically lasted several minutes, with the heating-spots maintained at peak or near-peak temperatures for at least 10 s (Fig. 2).

Temperatures were measured from wavelength of the incandescent radiation from heating the sample which was generally between 660–780 nm. Temperature measurements were processed using T-rax (software by C. Prescher; [github.com/CPrescher/T-Rax](https://github.com/CPrescher/T-Rax)) that allowed for selection of more accurate wavelength windows that best described a grey body fit of the incandescent intensity (Table S1). The current windows for wavelength and pixel (Table S1) best describes the fit emission spectra for each experiment. Upon expanding the wavelength window beyond 770 nm temperature estimates increase by  $< 100$  K. Although changes in pixels (representing position of the hotspot) can



lead to significant changes in temperature estimates (higher by up to  $> 500$  K) with higher difference between upstream and downstream temperatures along with a poor fit of the spectra. A narrow range of wavelength window to best describe the emitted spectra has also been seen previously in experiments on a similar chemical system as ours (Jackson et al. 2018, 2021), where a poor fitting of the spectral data beyond the range of 670–770 nm was found. In their LHDAC experiments, Jackson et al. (2021) assume the higher temperature between the upstream and the downstream side as the equilibrium temperature of the experiment considering any potential misalignment of hot spot with respect to the pinhole. Although, we find that choosing the higher

temperature does not agree with the equilibrium distribution of major elements like Si, O and Mg (discussed below). We assume the average temperature between the two sides as the equilibrium temperature of the experiment, and note the uncertainties associated with the measurement. Experimental temperature estimates provided in Table 1 are the average temperatures of the final melting temperature measurements (before quenching) collected on the upstream and the downstream sides. We acknowledge that there may be other uncertainties in addition to what we report such as that arising from small misalignment of the heated spot with respect to the detector or from possible temperature gradients inside the heated spot among other sources. Note that

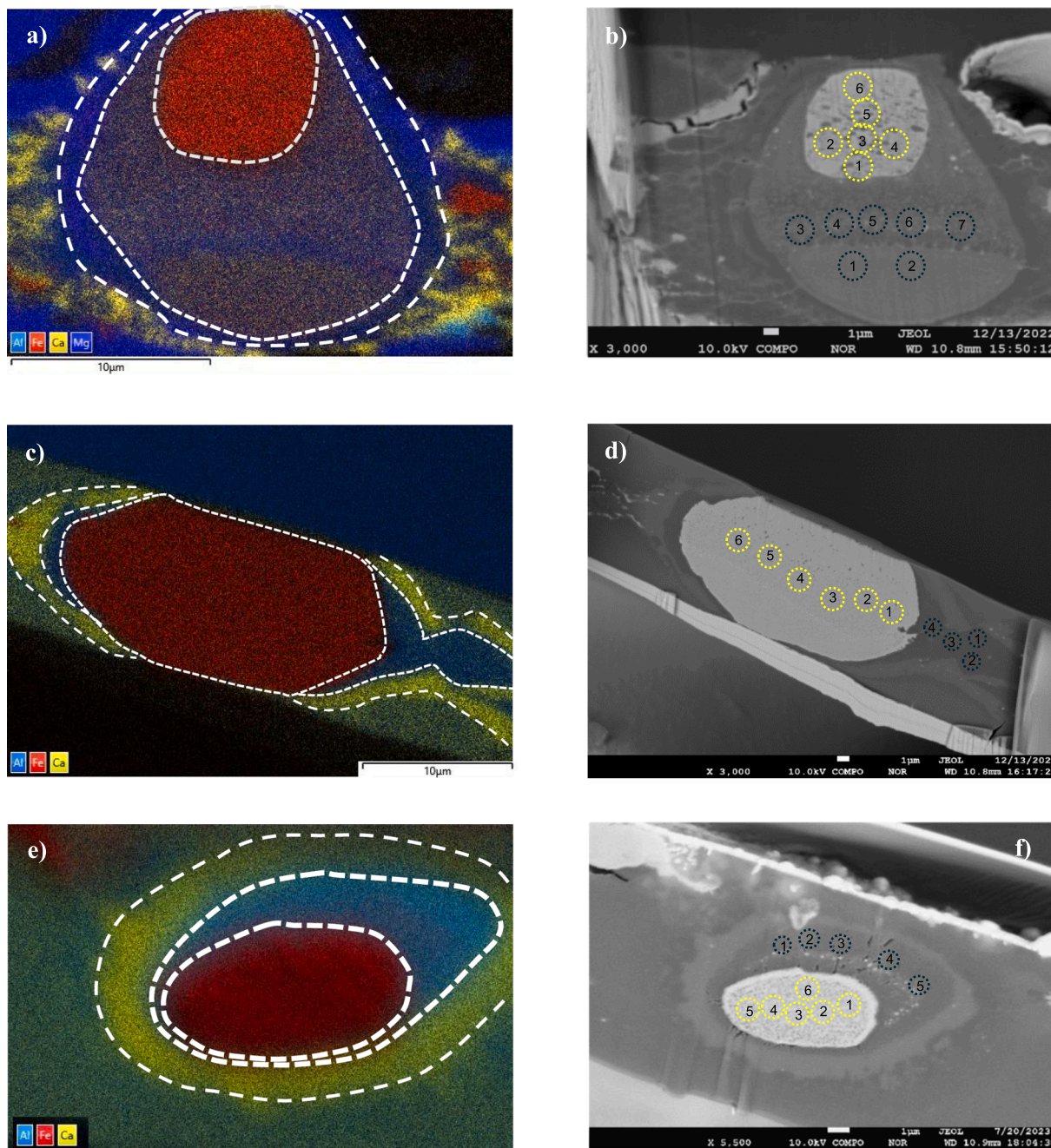


**Fig. 3.** SE images showing cross-sections of heated spots. (a) NMO50-3: [MgO-(iron nitride + glass)-MgO] designed experiment run at 69 GPa, 5794 K showing  $\text{MgSiO}_3$  crystallization (deep blue) around metal (red/brown)-silicate phases (light blue). (b) Compositional image for NMO50-3 (c) N49-1: [glass-iron nitride-glass] or nominal designed experiment run at 63 GPa, 5013 K showing  $\text{CaSiO}_3$  crystallization (yellow) around the metal-silicate phases. (d) Compositional image for (c). (e) N85-3: [glass-iron nitride-glass] run at 103 GPa, 5609 K. (f) Compositional image for (e). Dashed yellow circles are WDS measurement spots in metallic phase. Dashed blue circles are WDS measurement spots in silicate phase. Analytical values tabulated in Table S2 and S3 show average values of multiple measurements on the metallic or the silicate phase as shown in these figures, along with their standard deviations, for each heated spot.

each temperature measurement collected on either the upstream or the downstream are averages from a series of rapid measurements of the sample incandescence at the time of collection. The uncertainties of the temperature readings in Table 1 are the combined standard deviations of the final series of measurements taken on the upstream and the downstream. The recorded melting temperatures were used to account for thermal pressure ( $\Delta P_{th} = 2.7 \text{ MPa/K}$ , from Siebert et al., 2012) which is added to the recorded diamond edge pressure post heating to get the final pressures reported in Table 1.

## 2.5. DAC sample preparation for microprobe analysis

The DAC samples were then steadily decompressed at Tulane and preparations commenced for their chemical analysis. We first laser cut the Re around sample chambers to separate them from the remaining gasket, creating a disc nearly the diameter of the diamond culet. Marks for orientation were made on the Re portion of the discs and the discs were mounted on a TEM grid using a tungsten needle.

The heated spots (ref. as hot-spot) on these mounted samples were then cut open to expose a cross section that revealed the synthesized phases. This second step was done at LSU by using a focused ion beam (FIB) with a Ga source (Quanta 3D Dual Beam FEG FIB-SEM) and a plasma focused ion beam (PFIB) with a Xe source (Helios G5 CXe Plasma FIB). Both the instruments accelerate focused ions to mill the sample and explore the exposed cross sections. The PFIB was effective in making larger, coarser cuts at a 60 nA, 30 KeV ion beam current. This allowed for faster removal of the un-melted sample region. The Ga-FIB was then used to make smaller but finer cuts at 1–15 nA and 30 KeV ion beam current. The finer cuts allowed for a more careful survey of the phases being exposed when approaching a hot-spot. Exposure of a hot-spot (Fig. 3) was confirmed with secondary electron images.

## 2.6. Multi-anvil experiment

In addition to the DAC experiments, we ran a multi-anvil (MA) experiment at 15 GPa and 2773 K to corroborate our results obtained from LH-DAC experiments. We followed the sample assembly technique outlined in Righter et al. (2020) and ran the experiment in the 880 ton multi-anvil press at JSC using a 10/5 octahedra assembly. For our starting composition, we used the same 2:1 ratio of silicate + metallic alloy mix that was used for our MgO-saturated LH-DAC experiments. Additionally, we added a 1 wt% Si to the metallic alloy (iron nitride) to facilitate metal saturation. We loaded this starting composition into a single crystal MgO capsule. The sample was then heated following previously established power-temperature curves for the specific press and the sample assembly that we utilized (Fig. S2). Temperature was monitored using a type C W/Rh thermocouple up to a reading of 2373 K at which the thermocouple signal was lost. Heating of our sample beyond 2373 K to 2773 K was estimated using the resistivity of the heater, output power, and previous temperature calibration experiments on the same instrument. The experiment was held at 2773 K for ~ 5 min and quenched by shutting off power to the sample heating assembly. The quenched sample was later embedded in epoxy and polished using diamond pastes of increasing grit (up to 5000 grit or ~ 2  $\mu\text{m}$ ) for microprobe analysis.

## 2.7. Electron Microprobe Analysis

The exposed phases were analyzed for their silicate and alloy compositions at JSC using a JEOL 8530F Electron Probe Micro Analyzer. All samples were coated with Ir or Pt to facilitate the analysis of C. Prior to coating, each DAC sample was finely polished using a Ga-FIB (Quanta 3D) at low current. This polishing step was taken to remove any contaminants that had potentially accumulated on the surface since their initial milling and to further polish the sample surface. Polishing was completed with a 1 nA, 30 KeV ion beam. Once samples were polished

and coated, they were loaded into the vacuum chamber of the electron microprobe to limit accumulation of C, O, or H on the sample surfaces prior to their analysis.

We analyzed our samples following the approach in Jackson et al. (2021). The primary standards used for calibration were anorthite (for Al, Ca), San Carlos olivine (for Si, Mg), fayalite (for Fe, Si), stainless steel (for Fe, Ni),  $\text{Si}_3\text{N}_4$  (for N),  $\text{Fe}_3\text{C}$  (for C), and magnetite (for O). Peak intensities for elements of interest were quantified and were corrected for background X-ray intensity. Background was obtained through linear fitting of background intensity around the peaks of elements. Backgrounds and peak positions for light elements (N, C, O) used to quantify their concentrations are shown in Fig. S4. Count times for nitrogen was 90 s at peak position and 60 s for background, while that for other elements were 30 s and 15 s, respectively. We also analyzed the secondary standards, including volcanic glass (VG2), fayalite, San Carlos olivine, hyalophane, diopside, and magnetite. All secondary standards except hyalophane are Smithsonian microbeam standards. Nitrogen was measured on Hyalophane at  $0.11 \pm 0.02 \text{ wt\%}$  compared to a value of 0.12 wt% reported by Beran et al. (1992). We also analyzed stainless steel to measure the analytical precision and accuracy for alloy forming elements (C, N, Si). The blank concentration of nitrogen was < 0.01 wt% measured on nominally nitrogen free secondary standards magnetite, fayalite, diopside and San Carlos olivine. We then analyzed our samples for  $\text{SiO}_2$ ,  $\text{Al}_2\text{O}_3$ , FeO, MgO, CaO, N, and C in the silicate phases and Si, Al, Fe, Mg, Ca, N, C, and O in the metallic phases. Most analysis used a 10 KeV accelerating voltage and a beam current of 10 nA with a beam diameter of 1  $\mu\text{m}$  for the analysis of both silicate and metal phases. We also used variable beam current (3 nA and 5 nA) to confirm that nitrogen was not mobilized with variable beam densities. We measured nitrogen in our samples and the secondary standards on LDE1. The peak position for N was 146.8, identified on standard metal and silicate (Fig. S4). The nitrogen content in our silicate and metallic phases were higher (>0.42 wt%) than that remeasured on hyalophane, which gives us confidence on our silicate analysis of nitrogen (discussed below) using LDE1.

## 3. Results

### 3.1. Texture and composition of experimental products

We ran experiments varying as a function of pressure (and covarying temperature) and bulk composition (Table 1) to understand the effects of PTX on the partitioning of nitrogen between metal-silicate. Although we start with fixed bulk initial silicate and metal compositions within the respective designs (Fig. 2b and c), we get a wide variation in the silicate and the metal compositions across our samples post experimentation (Table 1, 2, 3; Fig. 5). This is likely caused from the small variations introduced to the silicate compositions from alumina contamination during ball milling (Fig. S1), the variable PT conditions of our experiment, and the local compositional domain sampled by the laser beam (~15–20  $\mu\text{m}$ ).

The experiments with both designs (Fig. 2 b and c) had a silicate phase (magma ocean equivalent) and a metallic phase (core) at the center of each hot-spot (Fig. 3), but the different designs yielded different textures, mineral phase assemblages surrounding the quenched silicate, and major element chemistry. The MgO-saturated experiments often had a layer of ferropericlase and/or bridgmanite encapsulating the silicate and metal phases (Fig. 3a). These experiments had depolymerized silicate melts with NBO/T values between 2.7 and 3.7 and were often associated with relatively coarse quench textures in the silicate phases (Fig. 3 a,b). Analysis of nitrogen concentrations in these silicate melts varied between 0.72–0.97 wt%, while the associated metallic domains had higher nitrogen concentrations between 5.07–10.55 wt%. In comparison, the nominal DAC designs had their metal and silicate phases mantled by a  $\text{CaSiO}_3$ -rich layer, likely davemaoite at the PT conditions of our experiments (Fig. 3b, Table 1). These experiments had more polymerized silicate melts with NBO/T ranging between 0.5–1.1.



**Table 2**  
**Silicate analysis** of our experimental data used for the formulation of Eq (7) Analysis and uncertainties are in wt%.

Sample	n	SiO <sub>2</sub>	Al <sub>2</sub> O <sub>3</sub>	FeO	MgO	CaO	N	Total <sup>a</sup>
N28-3	5	47.45 (0.41)	16.10 (0.21)	8.02 (0.40)	21.34 (0.74)	6.57 (0.20)	0.51 (0.12)	97.70
N32-2	6	41.29 (1.26)	18.67 (0.96)	12.55 (2.89)	18.11 (0.68)	8.03 (0.61)	1.34 (0.22)	99.08
N49-1	5	36.76 (1.59)	25.06 (0.50)	10.22 (3.02)	18.07 (0.25)	8.41 (0.26)	1.48 (0.15)	101.03
N65-3	6	42.88 (1.53)	25.47 (1.26)	7.96 (1.02)	15.06 (0.45)	6.42 (0.13)	2.21 (0.18)	100.28
N39-1	3	39.35 (0.46)	24.31 (0.60)	7.95 (0.35)	19.54 (0.18)	7.48 (0.22)	1.37 (0.39)	98.39
N39-2	8	43.35 (2.97)	20.29 (0.79)	14.39 (2.45)	13.65 (0.30)	6.99 (0.35)	1.33 (0.37)	99.51
NFO_2-2Fe-1	8	39.48 (0.74)	24.76 (0.16)	11.51 (0.64)	15.71 (0.18)	6.75 (0.11)	1.80 (0.24)	101.23
NFO_2-2Fe-2	4	34.27 (0.67)	29.10 (1.55)	6.65 (0.57)	19.95 (0.59)	7.97 (1.32)	2.06 (0.09)	103.25
NFO_2-4Fe-1	12	38.40 (2.39)	23.99 (1.23)	9.49 (3.29)	17.24 (0.52)	8.97 (1.54)	1.90 (0.27)	98.24
NMO50-3	7	24.29 (1.63)	10.84 (0.75)	26.79 (3.19)	33.10 (1.49)	4.12 (0.48)	0.86 (0.16)	88.98
NMO30-2	11	34.54 (0.94)	8.62 (0.22)	21.33 (0.70)	29.37 (0.34)	5.44 (0.12)	0.72 (0.07)	94.72
N75-1	4	39.30 (0.36)	28.87 (0.76)	11.08 (1.09)	14.73 (0.54)	3.90 (0.21)	2.11 (0.04)	101.59
N85-3	4	33.99 (0.79)	28.70 (0.73)	14.58 (2.54)	14.81 (0.42)	5.96 (0.21)	1.96 (0.15)	98.24
NFO_2-1Fe-1	5	43.76 (1.35)	22.77 (0.88)	9.65 (2.17)	15.25 (0.49)	6.28 (0.27)	2.29 (0.19)	100.75
NFO_2-1Fe-2	4	43.06 (1.05)	22.62 (0.29)	10.16 (0.49)	15.38 (0.25)	6.37 (0.15)	2.41 (0.10)	100.77
NMO50-1	6	28.92 (0.55)	10.85 (0.18)	24.44 (0.84)	30.37 (0.52)	4.45 (0.08)	0.97 (0.12)	93.59
N-MA-15-1	10	39.00 (1.81)	8.65 (0.86)	4.37 (0.61)	38.69 (3.53)	8.84 (1.51)	0.45 (0.17)	94.91

Note: a- Actual total measured on EPMA.

**Table 3**  
**Metal analysis** of our experimental data used for the formulation of Eq. (7) Analysis and uncertainties are in wt%.

Samples	n	Fe	Ni	N	C	Si	Mg	Al	Ca	O	Total <sup>a</sup>
N28-3	6	89.80 (0.62)	0.04 (0.08)	6.95 (0.08)	2.04 (0.39)	0.21 (0.02)	0.01 (0.01)	0.02 (0.01)	0.08 (0.03)	0.85 (0.06)	99.34
N32-2	6	86.40 (2.99)	0.08 (0.08)	5.79 (0.07)	2.60 (0.35)	2.59 (0.15)	0.08 (0.02)	0.12 (0.02)	0.12 (0.02)	2.23 (0.32)	96.39
N49-1	6	81.59 (1.06)	0.02 (0.03)	5.36 (0.37)	1.96 (0.51)	7.06 (0.39)	0.15 (0.01)	0.41 (0.03)	0.15 (0.03)	3.29 (0.25)	99.41
N65-3	5	78.53 (1.88)	0.07 (0.07)	6.04 (0.04)	3.96 (1.17)	7.29 (0.53)	0.13 (0.02)	0.41 (0.04)	0.20 (0.04)	3.37 (0.27)	96.10
N39-1	6	87.32 (0.56)	0.05 (0.06)	4.71 (0.25)	4.04 (0.25)	1.65 (0.08)	0.05 (0.01)	0.10 (0.01)	0.06 (0.01)	2.02 (0.08)	96.83
N39-2	6	82.20 (0.29)	0.06 (0.07)	4.99 (0.33)	4.20 (0.33)	3.94 (0.11)	0.14 (0.02)	0.30 (0.02)	0.15 (0.02)	4.03 (0.20)	98.22
NFO_2-2Fe-1	6	78.18 (2.18)	0.04 (0.02)	5.75 (0.42)	1.59 (0.43)	8.97 (0.55)	0.18 (0.06)	0.52 (0.18)	0.19 (0.03)	4.59 (0.80)	97.41
NFO_2-2Fe-2	4	82.37 (1.78)	0.06 (0.11)	7.34 (0.71)	1.73 (0.43)	5.19 (0.43)	0.12 (0.02)	0.33 (0.02)	0.22 (0.03)	2.64 (0.08)	98.09
NFO_2-4Fe-1	4	76.47 (1.93)	0.03 (0.04)	5.92 (1.11)	3.10 (0.32)	7.58 (1.17)	0.32 (0.08)	0.81 (0.25)	0.24 (0.03)	5.52 (1.60)	98.89
NMO50-3	6	78.72 (3.73)	0.05 (0.06)	5.07 (0.47)	6.27 (0.49)	0.59 (0.23)	1.21 (0.49)	0.24 (0.09)	0.22 (0.09)	7.64 (1.78)	94.73
NMO30-2	4	81.11 (1.95)	0.04 (0.04)	10.55 (0.44)	2.85 (0.11)	0.08 (0.06)	0.17 (0.07)	0.02 (0.02)	0.06 (0.01)	5.12 (0.25)	97.04
N75-1	4	75.02 (0.68)	0.05 (0.07)	6.42 (0.27)	2.07 (0.60)	9.35 (0.23)	0.28 (0.02)	0.86 (0.04)	0.21 (0.02)	5.75 (0.30)	95.72
N85-3	6	74.70 (2.42)	0.11 (0.11)	5.23 (0.27)	1.42 (0.55)	10.65 (0.67)	0.45 (0.07)	1.31 (0.10)	0.43 (0.02)	5.69 (0.58)	89.47
NFO_2-1Fe-1	5	78.95 (1.45)	0.03 (0.04)	5.76 (0.14)	3.84 (0.67)	6.37 (0.51)	0.25 (0.01)	0.56 (0.04)	0.22 (0.02)	4.03 (0.47)	95.18
NFO_2-1Fe-2	5	79.55 (0.34)	0.07 (0.1)	7.47 (0.33)	4.36 (0.53)	4.48 (0.15)	0.13 (0.01)	0.33 (0.04)	0.15 (0.01)	3.46 (0.28)	89.69
NMO50-1	4	79.90 (0.72)	0.09 (0.1)	8.97 (0.29)	2.84 (0.47)	0.14 (0.04)	0.28 (0.05)	0.06 (0.02)	0.10 (0.02)	7.61 (0.05)	93.75
N-MA-15-1	9	90.15 (0.42)	0.05 (0.06)	8.15 (0.42)	1.47 (0.20)	0.01 (0.02)	0.04 (0.04)	0.00 (0.00)	0.03 (0.03)	0.09 (0.13)	100.23

Note: a- Actual total measured on EPMA.

In addition, a stark difference between the two designs was also reflected in the O and the Si contents of the metallic domain, where the MgO saturated experiments had more O (up to 7.64 wt%), but the nominal designs had more Si content (up to 10.65 wt%). This gave us a wide

range of light element concentrations (O, Si) in our metallic domains over a relatively narrow PT space that enables us to more directly explore the effects of these elements on nitrogen siderophility. Carbon was present in our experiments, likely introduced as a contaminant, with

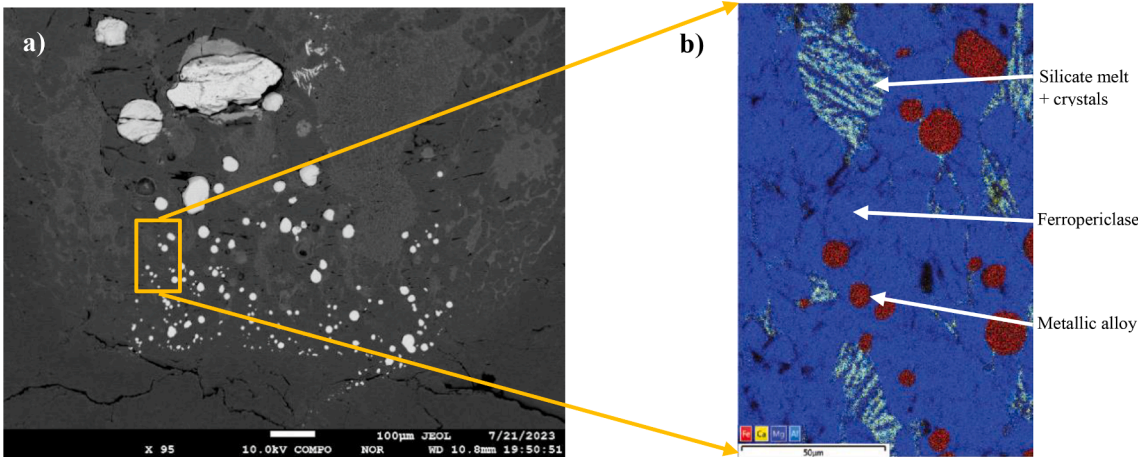


**Fig. 4.** A) BSE image of multi-anvil experiment run at 15 gpa and 2773 K. b) zoomed in EDS map of a region within the experiment showing distribution of metallic alloy (red), silicate melt and clusters of elongated MgO, (Mg,Ca)SiO<sub>3</sub> crystals, and ferropericlasite groundmass (blue).

up to 6.27 wt% in the metal, after removing blank concentrations of  $\sim 0.02$  wt% measured on stainless steel.

The multi-anvil experiment (Fig. 4) was MgO-saturated and displayed prominent quench textures with metallic blobs ( $<1 \mu\text{m}$  to  $100 \mu\text{m}$  in diameter) amidst the silicate mass. The relative coarse quench texture likely reflects the slower quench and relatively depolymerized composition of this experiment with an NBO/T value of 2.67. The silicate had elongated crystals of MgO and (Mg,Ca)  $\text{SiO}_3$  as seen in previously run MgO-saturated MA experiments (e.g., Richter et al., 2020).

Although we analyzed silicate domains that had relatively fine crystals, the major element concentrations (in wt%) of FeO, CaO and  $\text{Al}_2\text{O}_3$  had higher standard deviations ( $>0.5$  wt%) than that found in secondary standards ( $<0.4$  wt%). The MgO and the  $\text{SiO}_2$  contents (wt%) across the silicate phase had the most variation with standard deviations 3.5 wt% and 1.8 wt%, respectively which was likely due to sampling of different proportions of quench crystals. Nitrogen and carbon had a similar standard deviation (0.17 wt% and 0.26 wt%, respectively) across the silicate domain as found in the secondary standards (up to 0.14 wt% and

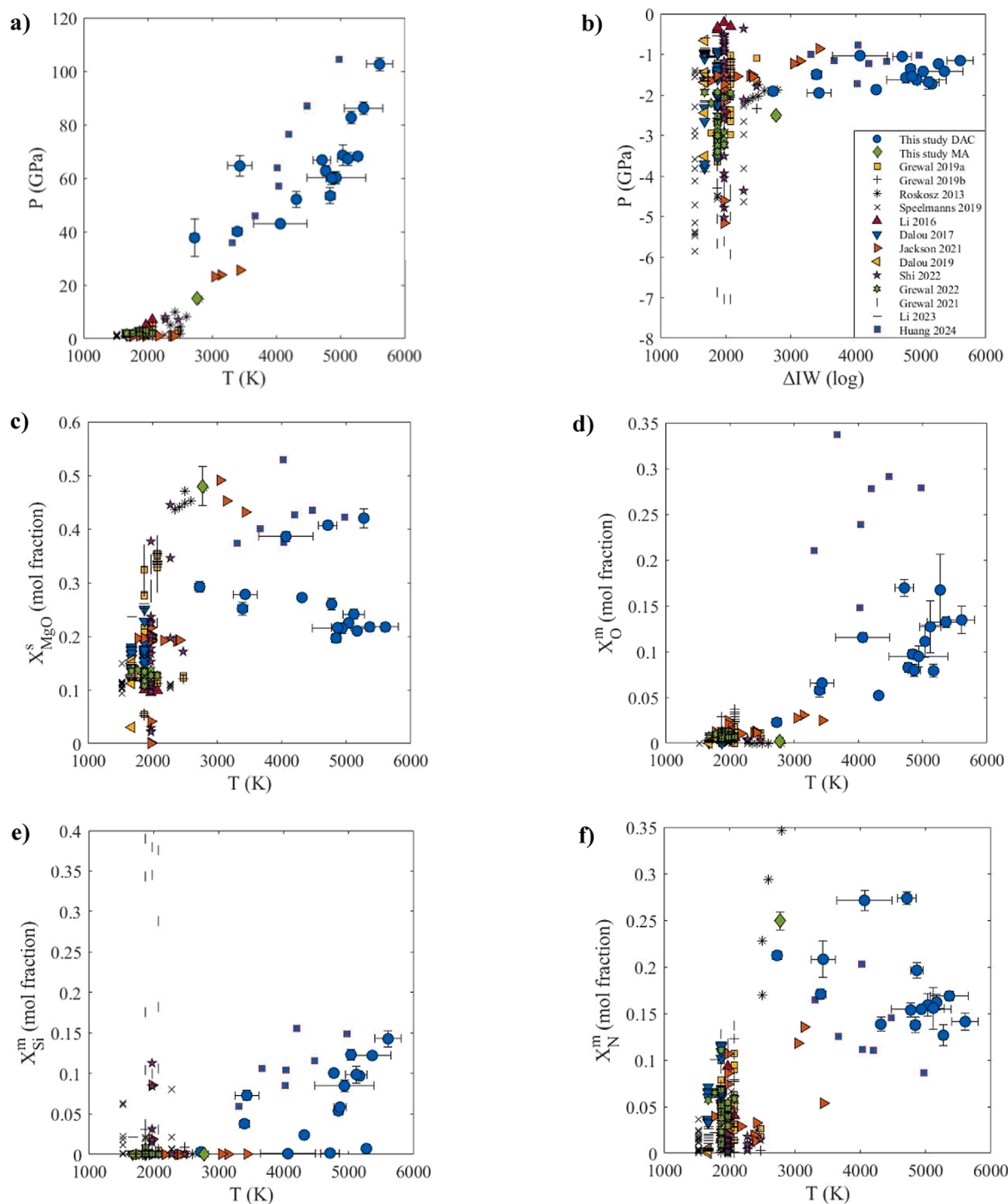


**Fig. 5.** PTX distribution of experimental data for nitrogen partitioning between metal and silicate. **a)** pressure–temperature distribution, **b)** oxygen fugacity vs temperature distribution, **c)** MgO content of silicate melt (melt chemistry distribution), **d)** O content in the metal, **e)** Si content in the metal. **f)** N content in the metal. Error bars for our data are analytical uncertainties calculated as 1-sigma around mean.



0.20 wt%, respectively). The average nitrogen concentration across the silicate domain was 0.45 wt%. For the metallic analysis, we measured blobs that were between 5–100  $\mu\text{m}$  in diameter (Fig. 4). The metal analysis showed more consistent concentrations of elements across the blobs with a maximum standard deviation of 0.42 wt% for the Fe concentration. The concentrations of Si, Al, Mg, and Ca were < 0.1 wt%, while the average nitrogen concentration in the metal 8.15 wt% with a standard deviation of 0.42 wt%. The measured oxygen concentration was below the blank concentration of 0.43 wt% measured on stainless steel.

### 3.2. PTX space explored by our new high-pressure data

We conducted successful experiments that investigated nitrogen partitioning between metal and silicate under previously unexplored PTX conditions (Fig. 5). It is important to note that PTX variables co-vary in our experiments, and any observed trends in Fig. 5 are likely influenced by these interdependencies. Our new high-pressure data spans a range of 15–103 GPa, similar to a recent study by Huang et al. (2024). However, our experiments achieved metal-silicate equilibrium over a broader temperature range and higher temperature (2728–5609 K,

Fig. 5a).

Oxygen fugacity of our LH-DAC experiments span between  $\Delta\text{IW}-1.03 \pm 0.02$  and  $\Delta\text{IW}-1.95 \pm 0.03$  while that for our multi-anvil experiment was  $\Delta\text{IW}-2.51 \pm 0.06$  (calculation described below, Fig. 5b). The narrow range of  $f\text{O}_2$  in our LH-DAC samples could be likely influenced by the homogeneity of starting metal and silicate compositions (except for variance in  $\text{Al}_2\text{O}_3$ ), the covarying effect of the experimental pressure and temperature on composition, and the abundance of oxidized and reduced compounds, some of which may be contaminants (e.g.,  $\text{H}_2\text{O}$ , organic carbon, FeO, Fe).

Our experiments produced a diverse range of silicate melts (Fig. 5c), enabling us to investigate the effect of silicate melt chemistry on nitrogen partitioning using LH-DAC. In terms of the depolymerization of the silicate melt, the silicate melts in our experiments have NBO/T between 0.5–3.8, due to the different experimental designs used in this study (Fig. 1). The metallic domains synthesized under the high temperatures conditions of our experiments allowed for greater incorporation of Si into the alloy than previously explored (Fig. 6a, b; 5d, e). The O content stable in our metallic alloy was higher than previous studies conducted below 20 GPa but was lower than the Huang et al. (2024) study conducted around similar pressure and oxygen fugacity as our experiments

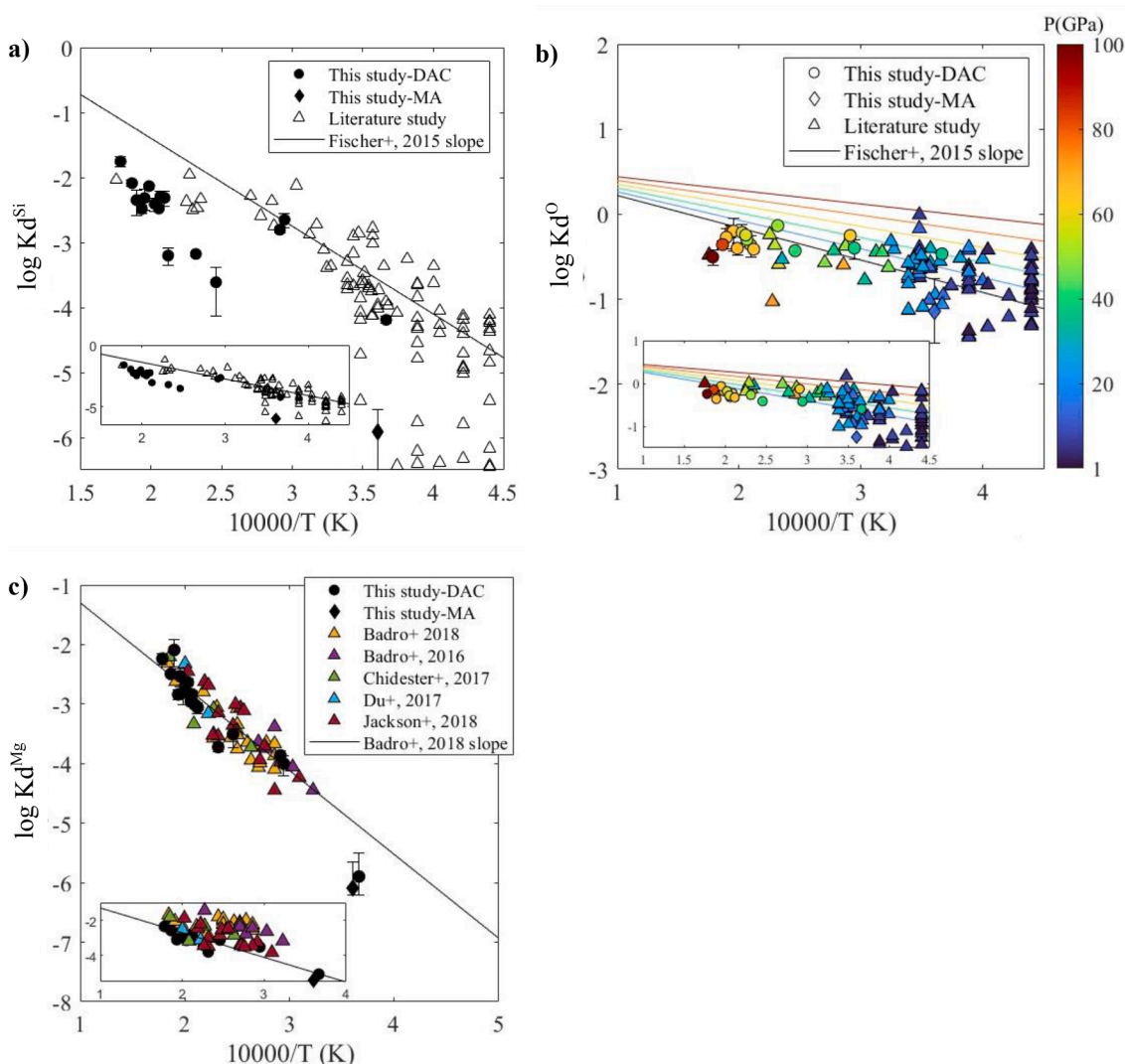


**Fig. 6.** Exchange coefficients of Si, O, Mg vs  $1/T$ . (a) Figure shows the comparison of  $K_d^{\text{Si}}$  values from this study (filled circles), model prediction from Fischer et al. (2015), and literature data recalculated for compositional effects. Inset shows raw data (no recalculation), (b) Figure shows comparison of compositionally recalculated  $K_d^{\text{O}}$  values from this study (filled circles) and literature values. Isobars were derived from model equation presented in Fischer et al. (2015). Inset shows raw data. (c) Comparison of compositionally recalculated  $K_d^{\text{Mg}}$  values from this study (filled circles) with literature data. Inset shows raw data.

(Huang et al., 2024). We stabilize high C in our alloy (1.42–6.27 wt%) over the range of high PT conditions of our experiments. In comparison, Huang et al. (2024) do not report any carbon in their experiments over similar pressure range as our experiments. Finally, our metallic chemistry also captured higher than previously explored nitrogen concentrations (Fig. 5f) likely due to nitrogen added as iron nitride in our starting composition.

The partition coefficient of nitrogen in our LHDAC experiments ( $D_N^{m/s}$ ) ranges between 12.29 ( $\pm 3.69$ ) and 1.70 ( $\pm 0.13$ ) and is 18.68 ( $\pm 9.02$ ) in our multi-anvil experiment. The  $D_N^{m/s}$  values suggest that nitrogen was moderately to slightly siderophile over the range of our PTX conditions. At face value, with the increase in the PT condition of our experiment,  $D_N^{m/s}$  seems to decrease suggesting that nitrogen tends to become less siderophile at higher PT conditions. There isn't any observable correlation between the raw  $D_N^{m/s}$  and the narrow range of oxygen fugacity in our experiments. The O and the Si contents of the alloy correlate negatively with the raw  $D_N^{m/s}$  of our experiment. Within the silicate melt domain, the MgO content of our melt correlates positively while the SiO<sub>2</sub> content correlates negatively with the raw  $D_N^{m/s}$  of our experiment. However, correlation of these raw data may be influenced by the covariance of the PTX parameters. To address this, we explore the independent effect of the parameters identified above on  $D_N^{m/s}$  and compare them with observations from literature below (see Discussion). The correlations of raw  $D_N^{m/s}$  and PTX parameters are shared in supplementary information (Fig. S6).

### 3.3. Determination of oxygen fugacity

Oxygen fugacity was estimated using the equation below, where  $\Delta IW$  represents  $fO_2$  calculated as log unit deviation from IW oxygen buffer.

$$\Delta IW = 2 \log \left( \frac{X_{FeO}^{silicate} \gamma_{FeO}^{silicate}}{X_{Fe}^{metal} \gamma_{Fe}^{metal}} \right)$$

The mole fractions of FeO and Fe are determined from analysis. We assume a  $\gamma$ -FeO of 1.25, similar to what was reported by O'Neill et al. (2002) for a MORB system. This assumption is used for our own data and the literature data when computing  $\Delta IW$  and parameterizing for  $D_N^{m/s}$  values below. The  $\gamma$ -Fe of our metallic alloy was evaluated using the Ma, (2001) formalism. This approach enables the application of interaction coefficients for alloying elements (Si, C, S, O) in predicting the non-ideality of Fe in Fe alloy. We use the interaction parameters ( $\epsilon$ ) for Si-Si, C-C, S-S, O-O, Si-C, Si-O, Si-S, C-O, C-S and O-S interactions from Badro et al. (2018). The equation below shows how  $\gamma$ -Fe is calculated for a N component metallic solution with Fe as the solvent and N-1 solutes (Si, C, S, O).

$$\begin{aligned} \ln \gamma_{Fe} = & \sum_{i=1}^{N-1} \epsilon_i^j (X_i + \ln(1 - X_i)) - \sum_{i=1}^{N-2} \\ & \times \sum_{j=i+1}^{N-1} \epsilon_{ij}^j X_i X_j \left( 1 + \frac{\ln(1 - X_i)}{X_i} + \frac{\ln(1 - X_j)}{X_j} \right) + \sum_{i=1}^{N-1} \\ & \times \sum_{j=1}^{N-1} \epsilon_{ij}^j X_i X_j \left( 1 + \frac{\ln(1 - X_j)}{X_j} - \frac{1}{(1 - X_i)} \right) + \frac{1}{2} \sum_{i=1}^{N-2} \\ & \times \sum_{j=i+1}^{N-1} \epsilon_{ij}^j X_i^2 X_j^2 \left( \frac{1}{1 - X_i} + \frac{1}{1 - X_j} - 1 \right) - \sum_{i=1}^{N-1} \\ & \times \sum_{j=1}^{N-1} \epsilon_{ij}^j X_i^2 X_j^2 \left( \frac{1}{1 - X_i} + \frac{1}{1 - X_j} + \frac{X_i}{2(1 - X_i)^2} - 1 \right) \end{aligned}$$

### 3.4. Demonstration of equilibrium

We evaluate equilibrium in our experiments by A) comparing the

distributions of Si, O, and Mg in our experiments with literature predictions, B) evaluating the spatial variation of major and minor element compositions across metal and silicate domains, and C) evaluating the characteristic diffusion length scales of elements in our experiments.

A) We explore the distribution of Si, O, and Mg in our metal-silicate experiments which have been well characterized up to high PT conditions (Badro et al., 2018; Fischer et al., 2015). Strong temperature dependency has been observed in the exchange coefficients of Si and the equilibrium constant associated with the dissociation of MgO (Badro et al., 2018; Fischer et al., 2015), while O has been suggested to exhibit both pressure and temperature dependencies on its metal-silicate partitioning (Fischer et al., 2015). Comparing the distribution of these elements in our experiments with predictions from the literature allowed for the evaluation of the accuracy of our chemical analysis and temperature determinations.

$Kd^{Si}$  (exchange coefficient for Si and Fe between metal and silicate) was determined given the following reaction: SiO<sub>2</sub> (silicate) + 2Fe (metal) = 2FeO (silicate) + Si (metal). Without any compositional recalculations (Fig. 6a inset), our data have a similar temperature dependency compared to the Fischer et al. (2015) model prediction but generally scatter below the model slope. We recalculate raw (no recalculation)  $Kd^{Si}$  values considering Si-O and Si-C interactions using  $\epsilon$  parameters from Fischer et al. (2015) and Steelmaking Sourcebook (1988), respectively. The recalculated  $Kd^{Si}$  values have small deviations from the raw values (Fig. 6a main). Note that our comparison in Fig. 6a does not account for the effect of Si-N interactions, and this effect is discussed below. The general scatter below the model prediction is consistent with Si repelling N in Fe alloy.

Values of  $Kd^O$  were computed based on the dissociation reaction: FeO (silicate) = Fe (metal) + O (metal). Compositionally recalculated values are plotted in Fig. 6b (main), while raw  $Kd^O$  values are plotted in the inset, (Fig. 6b inset). Our  $Kd^O$  values are correlated with temperature, with higher temperature being associated with higher  $Kd^O$  values, but our data do tend to plot below the isobars associated with our experimental pressures for both recalculated and raw data. Compositional recalculation of  $Kd^O$  values account for O-Si, O-C, and O-O interactions using the  $\epsilon$  parameters from Fischer et al. (2015) and Badro et al. (2015). As with Si, our comparison of  $Kd^O$  values does not account for the effect of O-N interactions. The general scatter below the model prediction is consistent with O repelling N in Fe alloy, as discussed below.

We also compared the  $Kd^{Mg}$  in our experiments with model predictions from Badro et al. (2018). We determined  $Kd^{Mg}$  based on the MgO dissociation reaction, where MgO (silicate) = Mg (metal) + O (metal). Values of  $Kd^{Mg}$  were recalculated for Mg-O, Mg-Si and Mg-C interactions using  $\epsilon$  parameters from the same work. There is good agreement of our recalculated  $Kd^{Mg}$  values with the model slope (Fig. 6c). One exception is N49-2 for which both the calculated exchange coefficients of Si and the equilibrium constant for the dissociation of MgO suggest colder temperatures than what we determined, scattering beyond the remainder of the data. This sample was therefore rejected from the dataset used for parameterizing  $D_N^{m/s}$  values. Taken together, our evaluations of Si, O, and Mg distributions in our experiments suggest that major element exchange between the metallic and silicate domains was efficient at our estimated temperatures and closely approach equilibrium conditions.

B) Another line of evidence for a close approach to equilibrium comes from the evaluation of compositional variation across the metal and the silicate domains in our experiments (Fig. 7) using WDS and EDS (Fig. 3). Under equilibrium conditions, there should be uniform compositions of the different phases in the assembly at a fixed PTX. Using WDS, we see variability between individual analysis of any given phase beyond the analytical precision of the microprobe (Fig. 7). This is likely due to sampling of quenched crystals by the electron beam within respective silicate and metallic domains. Quench crystals tend to form in both our experimental designs, with more depolymerized designs

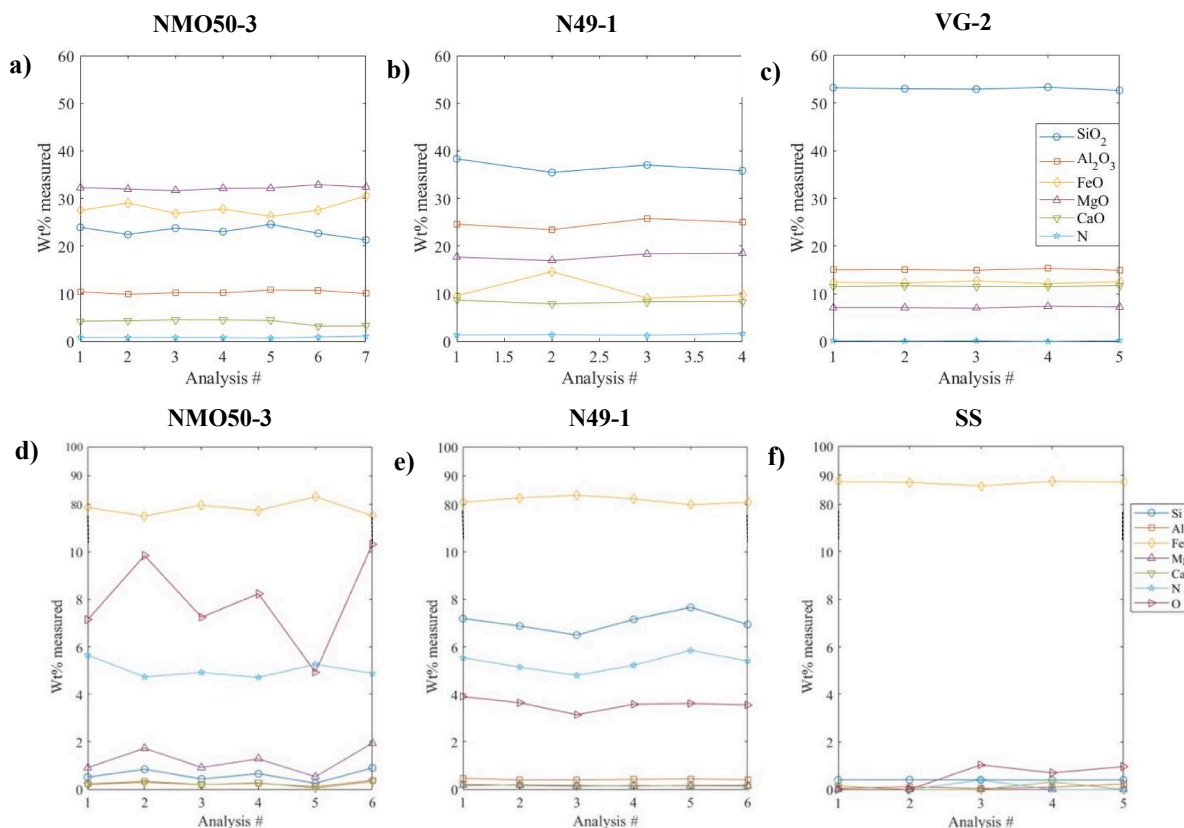


**Fig. 7. Microprobe (WDS) measurements across silicate** (a) NMO50-3, (b) N49-1, (c) volcanic glass (VG-2) **and metallic domains** (d) NMO50-3, (e) N49-1, (f) stainless steel (SS). NMO50-3 represents the MgO saturated experiments and N49-1 represents analysis of a nominal experimental design. Analysis numbers represent individual spots within the domains in Fig. 3. Volcanic glass and stainless steel are secondary standards used.

having coarser quench crystals. However, the average concentration of an element measured from multiple analysis across any given phase likely approaches the true chemistry of the phase. This is reflected in the equilibrium distribution of Si, Mg, and O between the metallic and the silicate domains as discussed above (Fig. 6). However, there is not any systematic variation of composition across the overall domains that would indicate disequilibrium conditions. Overall, the usage of a low keV beam (smaller activation volume), complete multiple analysis closer and further from distinctly separate phases (Figs. 3, 7) and the lack of systematic variation across a given phase (metal or silicate) demonstrate that we did not sample contaminants that would otherwise be indicative of disequilibrium chemistry.

**C)** We calculate the characteristic diffusion length scales for major elements in our metallic and silicate domains as a final evaluation for the approach to equilibrium in our experiments. Each experiment starts with unreacted materials that must exchange chemistry at high PT conditions to approach equilibrium over the heating duration. We calculate the diffusion lengthscale using  $L = 2\sqrt{Dt}$ , where  $D$  is the diffusion coefficient of an element and  $t$  is time. The large majority of our experiments were conducted above 4000 K and below 100 GPa, and within this PT window the diffusion coefficients of Mg, Si, and O are all found to be near  $10^{-9}$  m<sup>2</sup>/s or faster (Karki et al., 2010). Heating durations for our experiments varied but were always greater than 10 s (Fig. 2). The implied minimum diffusion length scale is 63  $\mu$ m in silicate. Similarly, diffusion coefficients for liquid Fe alloy are estimated to be  $10^{-7}$  m<sup>2</sup>/s or larger for the PT conditions of our experiments (Huang et al., 2019). The implied minimum diffusion lengthscale for major elements in our alloy is 200  $\mu$ m. In comparison the dimensions of our silicate and melt phases ( $\sim 5$ –20  $\mu$ m) are always smaller than our calculated diffusion length-scales, and this suggests that heating durations of our experiments were

sufficiently long enough for metal and silicate domains to exchange elements and approach equilibrium.

We admit that major element equilibrium does not require that N is in equilibrium, but for N to be in equilibrium in the system, the major elements must be in equilibrium since they influence the distribution of N in the system. It is difficult to conclude if the system was closed because the domain of the bulk composition sampled by laser beam is not exactly known. Although, we do not observe any N gradients within metallic or silicate phases from core to rim (Fig. 7), which would otherwise be suggestive of N loss to or gain from surroundings.

## 4. Discussion

### 4.1. Theoretical basis for parameterization of $D_N^{m/s}$

As established above, our dataset has expanded the PTX coverage of existing data for  $D_N^{m/s}$  values, and this permits the parameterization of these data to describe how  $D_N^{m/s}$  values vary in response to changes in intensive thermodynamic properties. Towards this end, we first assume that nitrogen in the silicate exists as  $N^{3-}$  as suggested by Libourel et al. (2003) for systems more reducing than IW and partitions as interstitial N atoms into the metal (Häglund et al., 1993) following the reaction below:



The equilibrium constant for this reaction can be written as:

$$K_N = \frac{(x_N^m)(aO^{2-})^{\frac{3}{2}}}{(x_{N^{3-}}^s)(fO_2)^{\frac{3}{4}}} = \frac{(x_N^m)(aO^{2-})^{\frac{3}{2}}}{(x_{N^{3-}}^s)(fO_2)^{\frac{3}{4}}} D_N^{m/s}, \text{ or}$$

$$\ln K_N = \ln \gamma_N^m - \ln \gamma_{N^{3-}}^s + \ln D_N^{m/s} - \frac{3}{4} \ln(fO_2) + \frac{3}{2} \ln(aO^{2-}) \quad (1)$$

where  $X_N^m$  and  $X_{N^{3-}}^s$  are mole fractions of nitrogen in the metal and silicate respectively and  $\gamma_N^m$  and  $\gamma_{N^{3-}}^s$  are the corresponding activity coefficients.  $D_N^{m/s}$  is the partition coefficient of nitrogen between metal and silicate and is expressed as  $D_N^{m/s} = \frac{X_N^m}{X_{N^{3-}}^s}$ .  $fO_2$  is the oxygen fugacity of the system. The  $aO^{2-}$  may vary according to melt composition. In our model formulation (Eq (7) below, any significant variations in  $aO^{2-}$  are captured by the parameters associated with the silicate melt model (SiO<sub>2</sub> regular solution).

By definition, equilibrium constant can be written as:

$$-K_N = \exp\left(\frac{\Delta H^0}{RT} - \frac{\Delta S^0}{R} + \frac{P\Delta V^0}{RT}\right) \quad (2)$$

Here,  $K_N$  is the equilibrium constant of reaction (1),  $\Delta H^0$ ,  $\Delta S^0$ , and  $\Delta V^0$  are the standard enthalpy change, entropy change and volume change of the reaction,  $R$  is the gas constant in J/mole/K, and  $T$  is temperature in K.

From Eq (1) and Eq (2) and with an assumption that  $\Delta H^0$ ,  $\Delta S^0$ , and  $\Delta V^0$  are constant across changes in  $P$  and  $T$ ,  $D_N^{m/s}$  can be re-cast as:

$$\ln D_N^{m/s} = a \frac{1}{T} + b \frac{P}{T} + c + \frac{3}{4} \ln(fO_2) - \ln \gamma_N^m + \ln \gamma_{N^{3-}}^s \quad (3)$$

$\gamma_N^m$  can be computed using the Ma, (2001) approach for a 'N' component system with Fe as the solvent and 'n-1' solutes:

$$\ln \gamma_N^m = \ln \gamma_{Fe}^m + \ln \gamma_N^0 - \frac{T_{ref}}{T} \epsilon_N^N \ln(1 - X_N) - \sum_{j=1}^{n-1} \epsilon_N^j X_j^{m'} \quad (4)$$

( $j \neq N$ )

Where  $\gamma_N^0$  represents the activity coefficient of nitrogen in the metal at infinite dilution,  $\epsilon_N^N$  is the nitrogen self-interaction parameter and  $\epsilon_N^j$  is the interaction parameter for the elements  $j = C, S, Ni, O$  or  $Si$  influencing nitrogen activity in the metal.  $T_{ref} = 1873$  K, the reference temperature at which most steelmaking  $\epsilon$  values are reported.  $X_j^{m'}$  takes the form:

$$X_j^{m'} = \frac{T_{ref}}{T} \left[ X_j \left( 1 + \frac{\ln(1 - X_j)}{X_j} - \frac{1}{(1 - X_i)} \right) - X_j^2 X_i \left( \frac{1}{1 - X_i} + \frac{1}{1 - X_j} + \frac{X_i}{2(1 - X_i)^2} - 1 \right) \right] \quad (5)$$

where  $X_{i,j}$  are mole fractions of the different elements in the alloy.

We assume  $\gamma_{N^{3-}}^s$  follows a symmetric regular solution model (e.g. Ghiorso and Carmichael, 1980):

$$\ln \gamma_{N^{3-}}^s = \sum_{j=1}^{n-1} \frac{\omega_N^j (X_j)^2}{RT} \quad (6)$$

( $j \neq N$ )

for a binary  $N^{3-} - i$  solution where  $i$  is a silicate melt component and  $X_i$  represents the mole fraction of this component other than  $N^{3-}$ .  $\omega_N^i$  is the regular solution parameter for this interaction,  $R$  is the gas constant in J/mole/K, and  $T$  is temperature in K.

#### 4.2. Model formulation

Eq (3) gives us the functional forms of PTX parameters that can explain the partitioning of nitrogen between metal and silicate. We then

compiled a global dataset (Dalou et al., 2017, 2019a; Grewal et al., 2019a, 2019b, 2021b, 2022b; Huang et al., 2024; Jackson et al., 2021; Li et al., 2023, 2016; Roskosz et al., 2013; Shi et al., 2022; Speelmanns et al., 2019) to parameterize  $D_N^{m/s}$  over a wider span of PTX conditions than what our study alone enables. For the Roskosz et al. (2013) dataset we assume zero carbon concentrations for the LH-DAC data and assume the deviation of the totals from 100 % as carbon concentrations for the MA experiments. Additionally, we do not include 7 data points from Grewal et al. (2019a) (discussed in Fig. S5) and one experiment PC\_NEXP3 from Jackson et al. (2021) with high Si (~13 wt%) in the metal at 0.95 GPa and 1973 K.

Since the alloy effects for N-C, N-S and N-Ni interactions have been systematically studied in earlier works (e.g., Grewal et al., 2019a, 2019b; Jackson et al., 2021; Roskosz et al., 2013; Shi et al., 2022), we recalculate the measured  $D_N^{m/s}$  values of our global data for these interactions. It is also necessary to recalculate for these effects considering the absence of these elements in some experimental studies that we include in our global database and their overall subtle effect on the global dataset. To recalculate, we subtract the term  $\epsilon_N^j X_j^{m'}$  from the measured  $D_N^{m/s}$  (log) using Eq (5) for C, S, and Ni and the interaction parameters from Jackson et al. (2021).

The C-, S-, Ni- recalculated  $D_N$  values were then fit against the other relevant parameters based on Eq (3) using a least squares approach. We evaluate the parameters based on their significance (p-value). The threshold for p-values was set at 0.05, and we did not consider parameters with  $> 0.05$  p-values. We started a model with  $1/T$ ,  $P/T$  and  $fO_2$  as our initial set of parameters based on the thermodynamic rationale presented in Eq (3). Oxygen fugacity, expressed as  $\Delta IW$ , had the lowest p-value ( $< 0.0001$ ) and gave an  $R^2$  of 0.62 alone.  $1/T$  followed as the subsequent significant term with a p-value  $< 0.0001$  and increased the  $R^2$  to 0.73. Bringing in the  $P/T$  term, however, had a high p-value ( $> 0.05$ ) and was not considered initially for the model.

We then explored the significance of different compositional parameters and their effect on the model fit. For the alloy chemistry effects, we explored the parameters  $\ln(1 - X_N) \frac{T_{ref}}{T}$  (annotated as  $X_N^{m'}$ ),  $X_O^{m'}$ ,  $X_{Si}^{m'}$ ,  $X_{Mg}^{m'}$ ,  $X_{Ca}^{m'}$ , and  $X_{Al}^{m'}$  to identify the alloy solute components that affect  $D_N^{m/s}$ . The  $X_j^{m'}$  values ( $j = N, O, Si, Mg, Ca, Al$ ) were calculated using Eq (5). The terms  $X_{Si}^{m'}$  and  $X_N^{m'}$  had the highest significance with p-values  $< 0.0001$  followed  $X_O^{m'}$  with a p-value of 0.01.  $X_{Mg}^{m'}$ ,  $X_{Ca}^{m'}$  and  $X_{Al}^{m'}$  had p-values  $> 0.05$  and were not included in the model. The overall model had an  $R^2$  of 0.78 at this step.

We evaluated the significance of our oxide parameters ( $i = SiO_2, Al_2O_3, MgO$  and  $CaO$ ) in their functional form  $\frac{\omega_N^i (X_i)^2}{RT}$ . We did not fit for FeO given its direct correlation with the  $\Delta IW$  term, already included in the model. Amongst our oxide parameters, we found that  $SiO_2$  and  $MgO$  have higher significance (p-values  $< 0.0001$ ) than  $CaO$  and  $Al_2O_3$ . The  $SiO_2$  and the  $MgO$  contents are anticorrelated in the experiments and can therefore be used interchangeably to capture the effect of silicate composition on N. However, choosing either  $SiO_2$  or  $MgO$  as the first significant silicate parameter had implications on the next choice of silicate parameters and on the slope of the already identified significant parameters. Choosing  $MgO$  as the first silicate parameter,  $CaO$  and  $Al_2O_3$  followed suit as the next silicate parameters. Each of these terms ( $MgO, CaO, Al_2O_3$ ) had positive coefficients, which suggested that their enrichment in the melt makes nitrogen more siderophile. With this choice of silicate parameters,  $SiO_2$  became less significant with a p-value of 0.0206. The model  $R^2$  value was 0.87 with this choice.

Choosing  $SiO_2$  as the first silicate parameter, on the other hand, yielded a negative coefficient and suggested that nitrogen becomes less siderophile with  $SiO_2$  enrichment in the silicate melt. The  $R^2$  of the model when choosing  $SiO_2$  as the significant silicate parameter was 0.84. Choosing  $SiO_2$  as the silicate parameter decreased the slope of  $\Delta IW$  from 0.54 to 0.39. This deviation further away from the  $\frac{3}{4}$  slope is



expected for a  $N^{3-}$  dominated speciation in the silicate melt. Given the choice of MgO or  $SiO_2$  to describe melt compositional effects, we selected  $SiO_2$ . Our decision here is driven by evidence for Si- $N^{3-}$  interactions in silicate melts (Huang et al., 2022a) that should act to stabilize nitrogen in the silicate and decrease its siderophility (consistent with the negative coefficient we retrieve from our fitting).

Finally, the P/T term became significant with a p-value of 0.0059 after considering the compositional terms discussed above, while the overall model  $R^2$  improved by 0.004. The significance of this term was independent of our choice for the silicate melt parameter.

With the 7 PTX parameters identified from the procedure described above our final model takes the form in Eq (7) with an  $R^2$  of 0.84.

$$\log D_N^{m/s} = \frac{5559.4(\pm 450.6)}{T(K)} + \frac{33.3(\pm 12.0)P(GPa)}{T(K)} + 0.39(\pm 0.02)\Delta IW - 5.46(\pm 1.29)X_N^{m'} + 8.72(\pm 2.66)X_O^{m'} + 9.05(\pm 1.04)X_{Si}^{m'} - 54023(\pm 5055)\left(\frac{X_{SiO_2}^s}{R.T(K)}\right)^2 - 0.11(\pm 0.22) \quad (7)$$

Note that Eq (7) is derived for systems without C, Ni, and S. To include these compositional effects in predictions we suggest adding interaction terms analogous to those given for oxygen or silicon, although this complicates propagation of uncertainties. For realistic estimations of  $D_N^{m/s}$ , we encourage using Eq (7) with all the PT and X parameters identified as having significant influences on  $D_N^{m/s}$ , to incorporate the effect of evolving chemistry of the system on  $D_N^{m/s}$ . The chemistry of metal (core) and silicate (mantle/MO) for a given PTX condition can be determined from the approach by Rubie et al. (2011){Citation}, which also allows for determination of  $fO_2$  of the system.

#### 4.3. Model parameters and their implications

Our model from Eq (7) allows for a refined understanding of the behavior of nitrogen during core formation (Fig. 3). Based on our model fits, we infer that pressure has a positive effect on the siderophility of nitrogen, while temperature has a negative influence on its siderophility (Fig. 8a). Our temperature sensitivity is similar to previous determinations (Grewal et al., 2019a; Huang et al., 2024; Jackson et al., 2021; Shi et al., 2022; Speelmanns et al., 2019). Although there is uniform agreement that higher temperatures make N less siderophile, there is more disagreement regarding the role of pressure in modulating nitrogen partitioning. The models presented by Dalou et al. (2017) and

Speelmanns et al. (2019) suggest negligible pressure effect between 1.2–3 GPa and 0.85–5.5 GPa, respectively, whereas models by Grewal et al. (2019a, 2019b) (1–6 GPa) and Shi et al. (2022) (1–8 GPa) report a positive effect of pressure on nitrogen's siderophility. Higher pressure behavior of nitrogen beyond 8 GPa was explored by Huang et al. (2024), Jackson et al. (2021) and Roskosz et al. (2013) but these studies had different conclusions on the effect of pressure. While Roskosz et al. (2013) did not observe any conclusive effect of pressure on  $D_N^{m/s}$  in their experiments conducted up to ~ 15 GPa, Jackson et al. (2021) ran experiments between 0.95–25.6 GPa and their model suggested that pressure increases the siderophility of nitrogen. Although, Huang et al. (2024) did not find the significance of pressure effect in their model which included higher pressure data up to 104 GPa. Our conclusion regarding the positive effect of pressure on nitrogen partitioning is enabled by the expanded PTX provided by our dataset.

We find that oxygen fugacity of the system has a positive effect on nitrogen siderophility, meaning more oxidized conditions favor nitrogen siderophility (Fig. 8b). This relationship qualitatively consistent with Reaction (1) and is consistent with other nitrogen metal-silicate partitioning studies (Dalou et al., 2019; Grewal et al., 2019a; Huang et al., 2024; Jackson et al., 2021; Li et al., 2016; Shi et al., 2022; Speelmanns et al., 2019). The coefficient we find for  $\Delta IW$ , however, is 0.39 ( $\pm 0.02$ ), much lower than the 0.75 slope predicted by Eq (3) for Reaction (1). The dependency of  $fO_2$  on other compositional parameters deemed significant in our model could influence this slope quantitatively. Although, a similar observation of ( $<0.75$  coefficient) has been seen in several other experimental studies as well (Jackson et al., 2021; Li et al., 2016; Shi et al., 2022; Speelmanns et al., 2019). Studies which do not have Si in their metallic alloy at  $< IW$  oxygen fugacity also fit to produce a  $\Delta IW$  coefficient of  $< 0.75$  (Dalou et al., 2019a; Li et al., 2023; Speelmanns et al., 2019) highlighting that the  $< 0.75$  coefficient is independent of the choice of parameters in Eq (7). A large deviation from the 0.75 slope may suggest the involvement of a  $N_2$  species as a solute component in the silicate phase or the stabilization of  $N^{3-}$  by  $Fe^{+2}$  dissolved in the melt. There is evidence from molecular dynamical work that  $N^{3-}$  does complex with  $Fe^{+2}$  and  $Si^{+4}$  under PT conditions relevant to this study (Huang et al., 2022a). Oxidizing and N-rich conditions promote  $N_2$  stability over  $N^{3-}$  and could require a different reaction to constrain nitrogen's partitioning, as below.



If  $N_2$  dominates the budget of N in melt then N partitioning would become insensitive to oxygen fugacity (Bernadou et al., 2021; Dasgupta

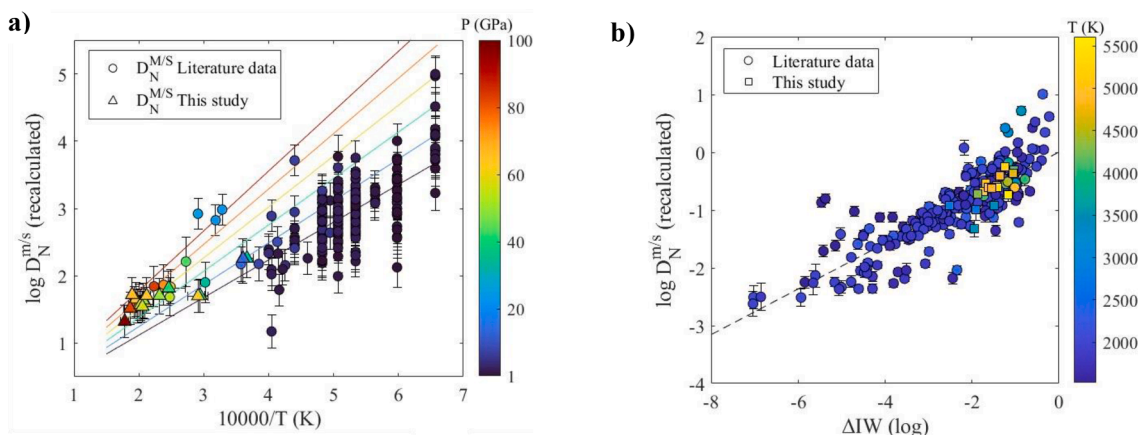


**Fig. 8.** A) Effect of pressure and temperature on  $D_N^{m/s}$ . Partition coefficients are recalculated for compositional effects using our model. The isobars are our model predictions of  $D_N^{m/s}$  considering the effects of pressure and temperature. Data on y-axis are recalculated to zero compositional effects and to IW. B) Effect of oxygen fugacity on  $D_N^{m/s}$ . Partition coefficients on y-axis are recalculated for the effect of P, T, and compositional effects other than oxygen fugacity using our model. Data points are color coded for the P or T they were acquired at. Error bars represent absolute uncertainties calculated from analytical uncertainties and recalculation assuming a normal distribution.

et al., 2022; Libourel et al., 2003; Mysen et al., 2014), lowering the coefficient of  $\Delta IW$ . Thus, there should be a PTX boundary where the Eq (7) is no longer valid. Experiments conducted under low PT conditions (up to 10 GPa and 1773 K) identify the redox boundary between  $N^{3-}$  and  $N_2$  dominated melt solubility near IW (Bernadou et al., 2021; Libourel et al., 2003). Although qualitatively, other studies also find this transition of N speciation around IW or more reducing conditions (Dalou et al., 2019b; Grewal et al., 2020; Mosenfelder et al., 2019). But it has not been defined for the PTX conditions associated with laser heated DAC studies (this study; Huang et al., 2024). Further systematic investigation of high PTX experiments is needed to find such a redox boundary and to evaluate the accuracy of our model in the  $N_2$  dominated conditions. This warrants caution on using our model at high PT conditions (>25 GPa, 2500 K) and oxidizing conditions close to IW where the effect of  $fO_2$  might be lower on  $D_N$ , as well as below more reducing conditions than  $\Delta IW -2$ , where limited experimental data exist.

Our model also suggests that the Si, O and N contents of the alloy influence the siderophilicity of nitrogen. We find that Si has a negative effect on nitrogen siderophilicity (Fig. 9a), as suggested by Grewal et al. (2019a), Shi et al. (2022), and Huang et al. (2024). Although, the magnitude of the slope determined by Grewal et al. (2019a) is different from that determined by Shi et al. (2022) and Huang et al. (2024) likely due to differences in the assumed structural form of the parameter in their models. These studies report slopes that do not scale with

temperature as the interaction parameter does (Ma, 2001), which when applied to the extreme temperatures associated with core formation may underestimate the partitioning of nitrogen into the core (overpredict strength of interaction between the element and N). Additionally, the temperature scaling of the different parameters are likely different and Si and O can be incorporated into alloy at different levels for a given temperature.

The interaction parameter based on our model fit for N-Si interaction ( $\epsilon_N^{Si}$ ) was  $9.06 (\pm 1.05)$ , determined for a reference temperature of 1873 K. Our N-Si interaction coefficient is fit with data that span a wide range of temperatures, and this provides confidence in using the  $1/T$  scaling assumed here for describing non-ideal solution terms. Application of the  $\epsilon_N^{Si}$  value in our model to any desired temperature considers temperature scaling of this interaction term as shown in Equations (4) and (5). Considering this  $\epsilon_N^{Si}$  value to compositionally recalculate the  $Kd^{Si}$  values from Fig. 6a, the recalculated  $Kd^{Si}$  values shift close to the slope predicted by Fischer et al. (2015) as shown in Fig. 10a.

Oxygen has a similar effect on nitrogen as Si, where the incorporation of oxygen into the alloy makes nitrogen less siderophile (Fig. 9b). Our finding is qualitatively consistent with the model from Huang et al. (2024) who also report a negative effect of oxygen on nitrogen siderophilicity. Although, the coefficient reported in their model does not scale with temperature. The interaction parameter for N-O interaction in the metallic alloy ( $\epsilon_N^O$ ) based on our model fit was  $8.72 (\pm 2.68)$ ,

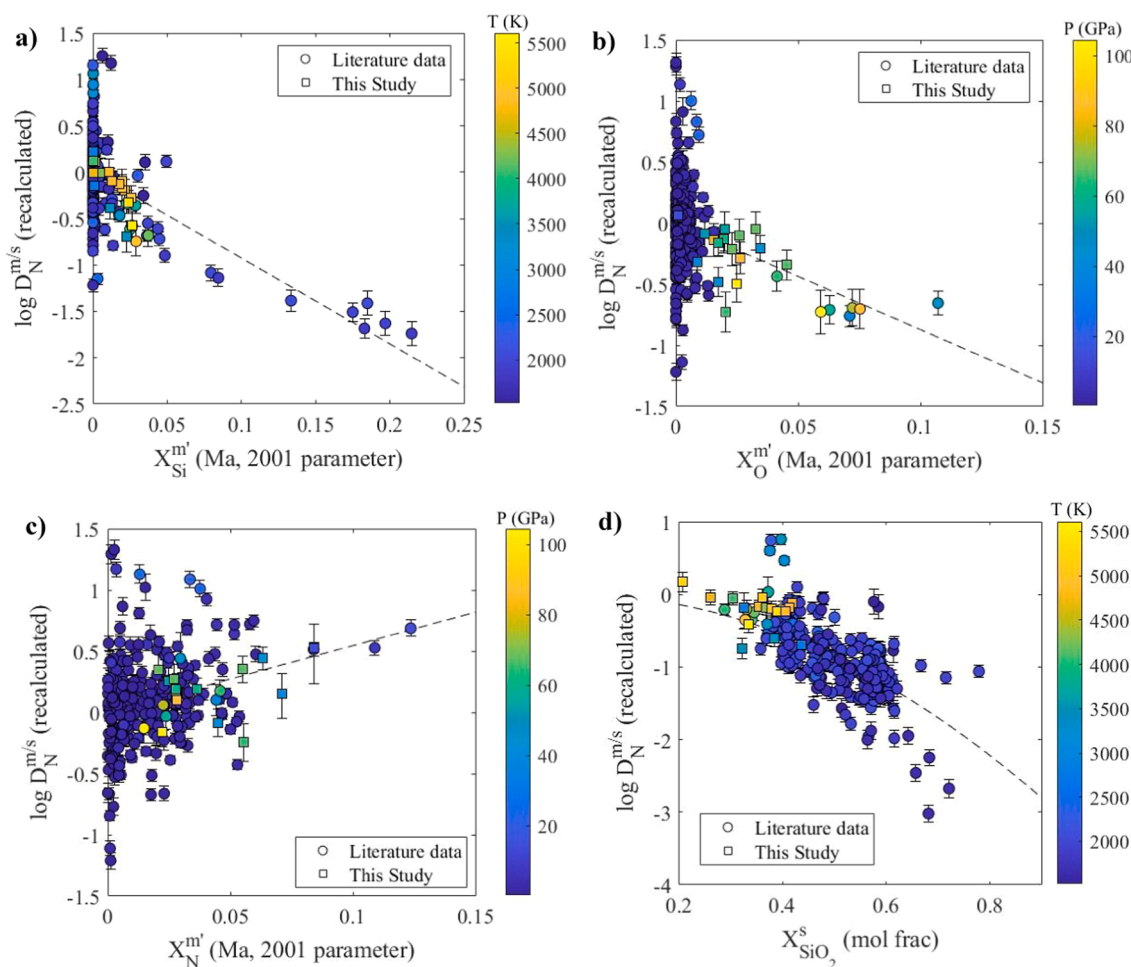


**Fig. 9.** Effect of alloy and silicate chemistry on  $D_N^{m/s}$ . **a)** Si content and **b)** O content in the metallic alloy make nitrogen less siderophile. **c)** N enrichment in the alloy makes nitrogen more siderophile. **d)**  $SiO_2$  enrichment in the silicate makes nitrogen less siderophile. X-axis represents alloy parameters of N, O and Si calculated using the Ma, (2001) approach considering the N-N, N-O and Si-N interactions. Data on y-axis are recalculated to no PTX effects and to IW except for the parameter on the respective x-axis in their functional form. Data points are color coded for the P or T they were acquired at. Error bars represent absolute uncertainties calculated from analytical uncertainties and compositional recalculation assuming a normal distribution.

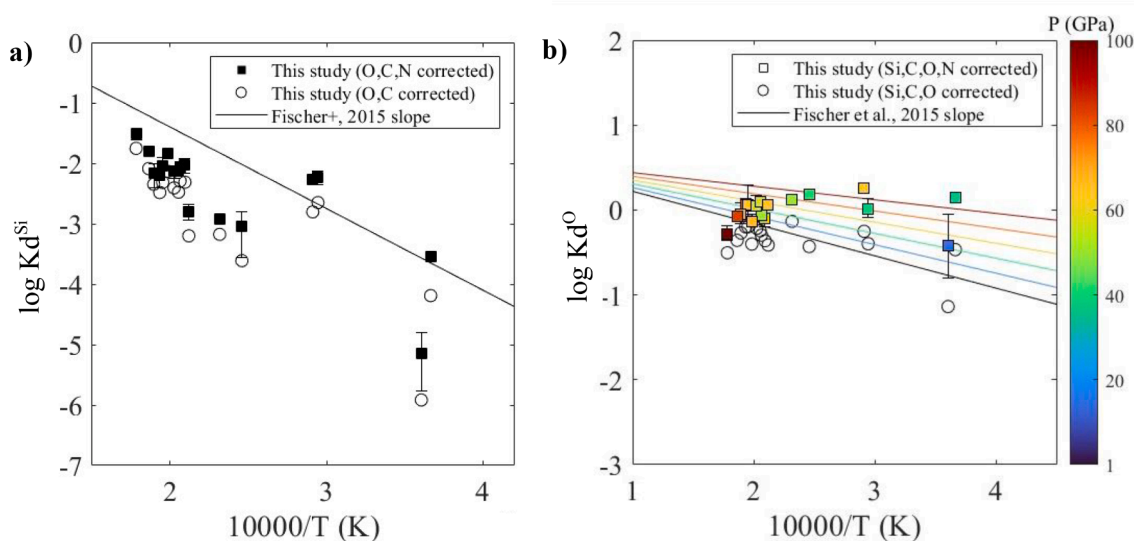


**Fig. 10.** A)  $\log Kd^{\text{Si}}$  recalculated for N-Si interaction. B)  $\log Kd^{\text{O}}$  recalculated for N-O interaction.  $\epsilon_N^{\text{O}}$  and  $\epsilon_{\text{Si}}^{\text{O}}$  values were based on our model fits in Eq (7). Error bars are absolute uncertainties calculated from analytical uncertainties.

determined for a reference temperature of 1873 K. Application of this term in our model considers temperature scaling like  $\epsilon_N^{\text{Si}}$  does above. We used this  $\epsilon_N^{\text{O}}$  value to compositionally recalculate for N-O interaction in Fig. 6b. The  $Kd^{\text{O}}$  data recalculated for N-O interaction shifts up towards the model predictions from Fischer et al. (2015), despite observable differences from the trend predicted by Fischer et al. (2015) (Fig. 10b).

In contrast to the effect of Si and O, the negative self-interaction coefficient,  $\epsilon_N^{\text{N}}$ , of 5.35 ( $\pm 1.56$ ) suggests more siderophile behavior with increasing the concentration of nitrogen in metal (Fig. 9c). Experimental systems tend to have high nitrogen concentrations (Fig. 5f), and thus the N-N interaction parameter suggests current data are biased to high  $D_N^{\text{m/s}}$  values when applying to natural systems with low nitrogen concentrations.

Lastly, our model predicts that the  $\text{SiO}_2$  content of the silicate makes nitrogen less siderophile (Fig. 9d). The effect of silicate melt has been quantified as NBO/T in previous studies (Grewal et al., 2019a; Huang et al., 2024; Shi et al., 2022), which proxies for the structure of the silicate melt. Although, the melt structure varies with pressure and temperature, as well as composition (e.g. Huang et al., 2022b). Nonetheless, there are discrepancies on the effect of NBO/T on nitrogen siderophility. Speelmanns et al. (2019) do not observe any significant effect of the NBO/T within the range of their silicate melt composition (0.1–1.3). Grewal et al. (2019a) model the effect of NBO/T within a range of 0.4–2.5 and report a positive effect on nitrogen siderophility. Shi et al. (2022) observe a similar effect within an NBO/T range of 0.02–3.1, suggestive of a greater siderophile behavior with a more depolymerized melt. This positive correlation is also corroborated by Huang et al. (2024) who explored relatively depolymerized melts with NBO/T ranging between 2.4–3.2. Our experimental designs allow us to explore the effect of silicate melt composition over a wide range of melt polymerization (Fig. 11) with the nominal designs having a range of NBO/T between 0.5–1.1 and the MgO saturated designs between 2.7–3.7. We see a similar correlation with NBO/T in our experiments as Grewal et al. (2019a), Shi et al. (2022) and Huang et al. (2024), where the MgO-saturated experiments tend to witness a greater siderophile behavior of nitrogen than the nominal designs (Fig. 11). Though NBO/T correlates with silicate melt composition as a broader term, it does not reflect the chemical interaction that nitrogen has within the melt. Furthermore, studies using molecular dynamics now provide clues regarding specific interactions that nitrogen has in the melt (e.g. Huang et al., 2022a). Our model captures this chemical interaction with  $\text{SiO}_2$  in the melt and suggests that N-Si interaction in the silicate melt makes

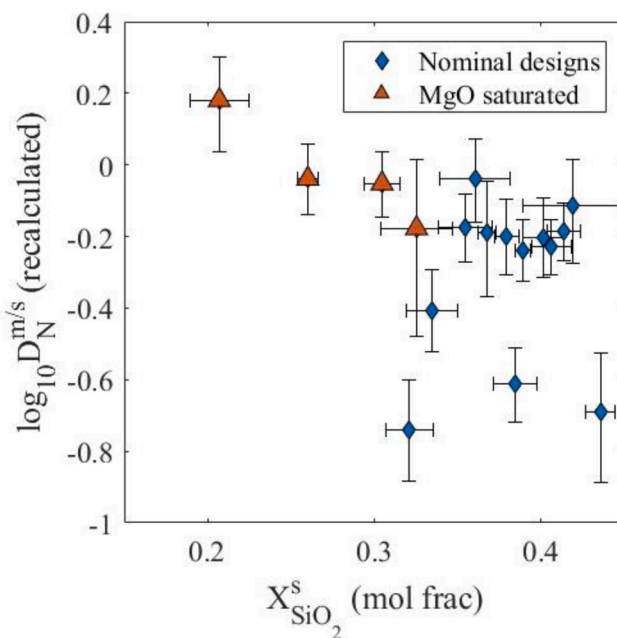


**Fig. 11.** Effect of melt composition on  $D_N^{\text{m/s}}$  across different experimental designs. Partition coefficients are recalculated to IW and for no P, T, X effects except for the effect of  $\text{SiO}_2$ . Error bars on x-axis represent analytical uncertainty. Vertical error bars are calculated by propagating analytical uncertainties through PTX recalculations based on Eq (7).

nitrogen less siderophile (Fig. 9d). Although, as discussed above, different silicate melt models yield similar quality of fits to the data, and we favor using  $\text{SiO}_2$  given the evidence for Si-N interactions in reduced melts (Huang et al., 2022a) and the relatively simple functional form. Lower  $\text{SiO}_2$  melts are associated with more siderophile behavior for N, and this is qualitatively consistent with Si-N interactions helping to stabilize N in melt. Additionally, the functional form considers scaling of the symmetric regular solution parameter  $\omega_N^{\text{SiO}_2}$  with temperature (Eq (6), unlike NBO/T.



#### 4.4. Model Validation

We used our model from Eq (7) to predict nitrogen partitioning in our multi-anvil experiment. The multi-anvil experiment was run at 15 GPa and 2773 K, a PT location that has relatively sparse data in the global compilation (Fig. 8a) and utilizes a method that is distinct from the majority of experiments used to determine our parameterization. Predicting nitrogen partitioning in this experiment, external to our global compilation, allowed us to evaluate the consistency of our model beyond where there is dense PTX coverage. Our model prediction falls within 95 % confidence interval of the observed partition coefficient of the MA experiment (Fig. 12). The success of our model to predict  $D_N^{m/s}$  values in PTX regions with relatively poor data coverage and with distinct methodology provides confidence in applying Eq (7) to natural systems. Adding the MA experiment to the global compilation does not affect parameters values or identify additional significant parameters.

#### 4.5. $D_N^{m/s}$ variations across PTX conditions

With Eq (7) established, we can now better predict the behavior of nitrogen in an accreting proto-Earth. Core formation likely proceeded from early episodes dominated by low PT conditions to later episodes where more extreme PT conditions prevailed (e.g. Canup and Asphaug, 2001; Tonks and Melosh, 1993). We apply our  $D_N^{m/s}$  model to core formation scenarios assuming a mantle liquidus from Fiquet et al. (2010) to constrain potential PT conditions of metal-silicate reaction (Fig. 13a). We apply the formalism in Rubie et al. (2011) to predict the major element chemistry of metal and silicate reacting over the range of PT conditions considered here and apply their “reduced” and an “oxidized” bulk planet compositions. Graphical representations of the mantle liquidus used here along the oxygen fugacity of the “reduced” and the “oxidized” bulk planet compositions are shared in supplementary material (Fig. S7).

Predicted  $D_N^{m/s}$  values for a “reduced” protoplanet are less than one (lithophile) across the PT conditions we explore in Fig. 13a. Low PT conditions produce a more pronounced lithophile behavior of nitrogen, while  $D_N^{m/s}$  values shift marginally higher as PT conditions increase. The

overall lithophile behavior of N throughout the PT range in Fig. 13a for a reduced protoplanet reflects that the net effect of the rise in Si and O with increase in temperature (forcing  $D_N^{m/s}$  down) remain roughly balanced by the rise in the oxygen fugacity ( $\Delta IW$ ) of the system and pressure (forcing  $D_N^{m/s}$  up) in a reduced protoplanet system.

Predicted  $D_N^{m/s}$  values for an “oxidized” protoplanet decrease by approximately an order of magnitude across the PTX range of conditions associated with these scenarios (Fig. 13a). Oxidizing conditions promote higher  $D_N^{m/s}$  values under low PT conditions, but as PT conditions increase, the effects of temperature, Si and O content work to drive down  $D_N^{m/s}$  values, more than offsetting the effects of pressure and oxygen fugacity. We predict little difference in  $D_N^{m/s}$  values above 100 GPa between oxidized and reduced protoplanets.

Upon applying the nitrogen partitioning model from Huang et al. (2024) to the PTX space explored in Fig. 13a we observe similar trends of the predicted  $D_N^{m/s}$  values across both the “oxidized” and the “reduced” systems (Fig. 13b, c), where the siderophilicity of nitrogen decreases with increasing PT conditions. In both scenarios, their predicted  $D_N^{m/s}$  values have smaller differences from our model predictions at low PT but at high PT conditions their predictions suggest an order of magnitude lower siderophilicity of nitrogen than what our models predict. Note that we assume zero C and S and an NBO/T value of 2.6 to predict  $D_N^{m/s}$  using the Huang et al. (2024) model.

#### 4.6. Elemental fractionations of VSEs by core formation

We now apply Eq (7) towards understanding how N and other VSEs are redistributed during terrestrial planet accretion. There are varying ideas on the concentration of VSEs in BSE, specifically regarding the apparent depletion of nitrogen with respect to hydrogen, sulfur and carbon, when normalized to CI chondrite (Halliday, 2013; Hirschmann, 2016; Marty, 2012; Wasson et al., 1997; Johnson and Goldblatt, 2015; Yoshioka et al., 2018). Although, CI chondrites and the Sun are more similar in composition for the refractory elements, CI chondrites show differences in their volatile inventory (Anders and Grevesse, 1989; Lodders, 2003; Palme et al., 2014). CI chondrites themselves have different distributions of VSEs when compared to the other primitive chondrites (Hirschmann et al., 2021; Marty et al., 2020). Furthermore, the volatile inventory of differentiated planetesimals exhibits a different range of VSE budgets and may even have a greater extent of VSE fractionation than the primitive, yet volatile rich chondrites (e.g. Grewal et al., 2022a). It is clear that many processes can fractionate VSEs as witnessed by the variable VSE ratios of primitive materials like chondrites as well as in more evolved planetesimals (e.g., Bergin et al., 2015; Hellmann et al., 2020; Vollstaedt et al., 2020). We focus here on the ability of core formation to induce VSE fractionations on the silicate portions of larger terrestrial bodies such as Earth.

To explore how core formation can induce VSE fractionations we first compare our predicted  $D_N^{m/s}$  values with the partition coefficients of other VSEs (C and S) with increasing PT conditions for core-formation in an “oxidized” and a “reduced” system (Fig. S7 a, b). We take the exchange coefficient model of carbon from Blanchard et al. (2022) for both possible + 2 and + 4 valence states of carbon. We also use the Eq (1) from Fischer et al. (2020) to predict  $D_C^{m/s}$  which includes the effects of  $\Delta IW$ , light elements in the alloy (O and S) and NBO/T on carbon partitioning in addition to PT terms. We assume sulfur-free calculations of  $D_C^{m/s}$  when using this equation and assume an NBO/T value of 2.6. The partitioning of sulfur ( $D_S^{m/s}$ ) was calculated using Eq S-8 from Jackson et al. (2021) assuming a carbon free system and the activity coefficient of Fe as one. We focus on C/N and S/N ratios because carbon and sulfur are relatively well studied under higher PT conditions compared to H (Blanchard et al., 2022; Dalou et al., 2017; Fischer et al., 2020; Grewal et al., 2019b; Jackson et al., 2021; Tagawa et al., 2021). The predicted C and S partition coefficients are plotted in Fig. 13 b and c. C and S remain siderophile across the PTX space of core formation, although they exhibit a lowering of this siderophile tendency with increasing PT

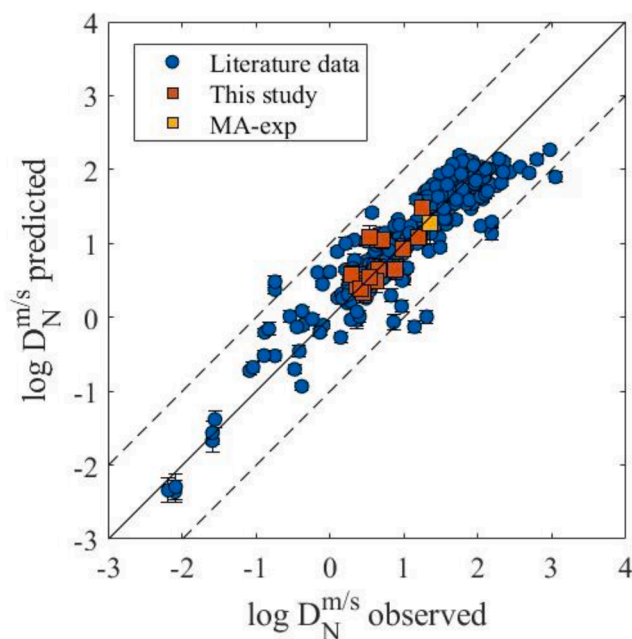


Fig. 12. 1:1 comparison of Model based  $D_N^{m/s}$  predictions from eq (7) on y-axis with the measured (observed)  $D_N^{m/s}$  values on the x-axis. The  $R^2$  of the regression is 0.85. MA-exp is the multi-anvil data that was not included in our model formulation of Eq (7).



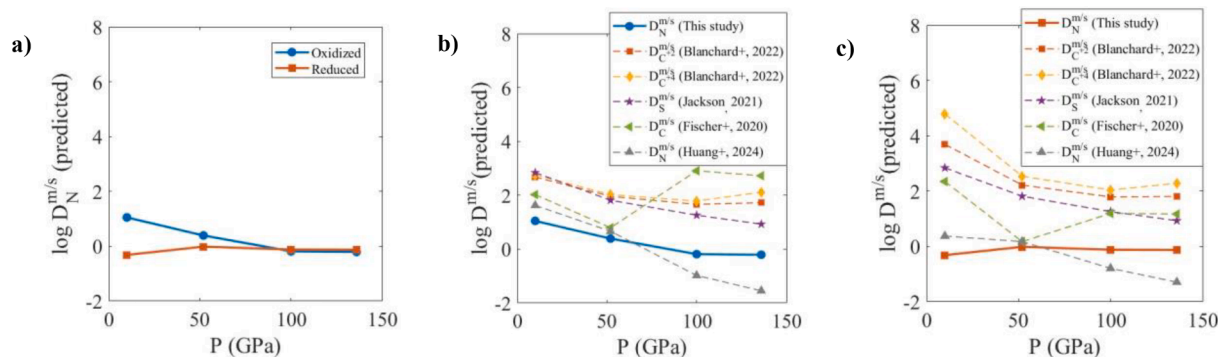


Fig. 13. A) application of nitrogen partitioning model to core formation for an oxidized system and a reduced system. Partition coefficients of N, C, H, and S across core formation PT conditions for b) oxidized protoplanet scenarios c) reduced protoplanet scenarios.

conditions. Nitrogen, in comparison, has a lower preference for the metallic alloy across the PTX span regardless of the oxidation state of the system.

We now apply the VSE partition coefficients to a *two-stage core formation model*. Our model is intended to evaluate how metal-silicate reactions associated with differentiated bodies impacting into a nearly fully grown Earth can fractionate VSE ratios. N-body simulations suggest that this type of interaction was relatively common during the giant impact stage of planetary growth (e.g., Agnor et al., 1999; Canup and Asphaug, 2001; Wetherill, 1985).

In the *first stage* we react metal and silicate of the impactor at 10 GPa and 2500 K for the “reduced” protoplanets and “oxidized” protoplanets at oxygen fugacity of  $\Delta IW$ -3.7 and  $\Delta IW$ -1.7, respectively to simulate core formation within smaller protoplanet bodies. We calculate the composition of metal and silicate under equilibrium within this smaller body using the batch equation as follows:

$$[i]_{\text{metal}} = \frac{D_i^{m/s} \cdot [i]_{\text{bulk}}}{D_i^{m/s} + (1 - D_i^{m/s}) f_{\text{silicate}}}$$

$$[i]_{\text{silicate}} = \frac{[i]_{\text{bulk}}}{D_i^{m/s} + (1 - D_i^{m/s}) f_{\text{silicate}}}$$

Here,  $[i]$  is the element N, C or S,  $D_i^{m/s}$  is the partition coefficient of the element and  $f_{\text{silicate}}$  is the mass fraction of the silicate phase that is in

equilibrium with the reacting metal. We assume bulk 1 wt% S, 1 wt% C and 100 ppm N (although only N partitioning depends on N concentration) and that the core is 1/3 of the overall protoplanet mass. Note that our model is focused on how VSE are fractionated, rather than predicting absolute concentrations, so the bulk concentrations of C and S are essentially placeholders.

In the *second stage* we then take the equilibrated core chemistry from the first stage calculation and let it backreact with a deep magma ocean (100 GPa, 5000 K), also exploring “reduced” and “oxidized” protoplanet scenarios to set the VSE partition coefficients for these more extreme conditions. In this second stage scenario, the “reduced” and the “oxidized” bulk systems have oxygen fugacity of  $\Delta IW$ -1.5 and  $\Delta IW$ -1.2, respectively, under the extreme temperatures of the second stage. The goal for this step is to calculate the chemical consequences of a smaller differentiated body accreting to a nearly Earth-sized differentiated body. We assume the magma ocean of the nearly Earth-sized body is devoid of VSEs, and any VSE present from its earlier growth stages is retained in the core, before reacting with the core from the first step. Details of the first stage and the second stage calculations are included in [supplementary information](#).

Fig. 14a plots predicted C/N and S/N ratios of the magma ocean against the metal/silicate ratio associated with core backreaction (i.e., the second stage) for the “reduced” protoplanet scenario. VSE ratios are normalized to their bulk ratios associated with the first stage calculation. We take the metal/silicate ratio associated with backreaction as a free

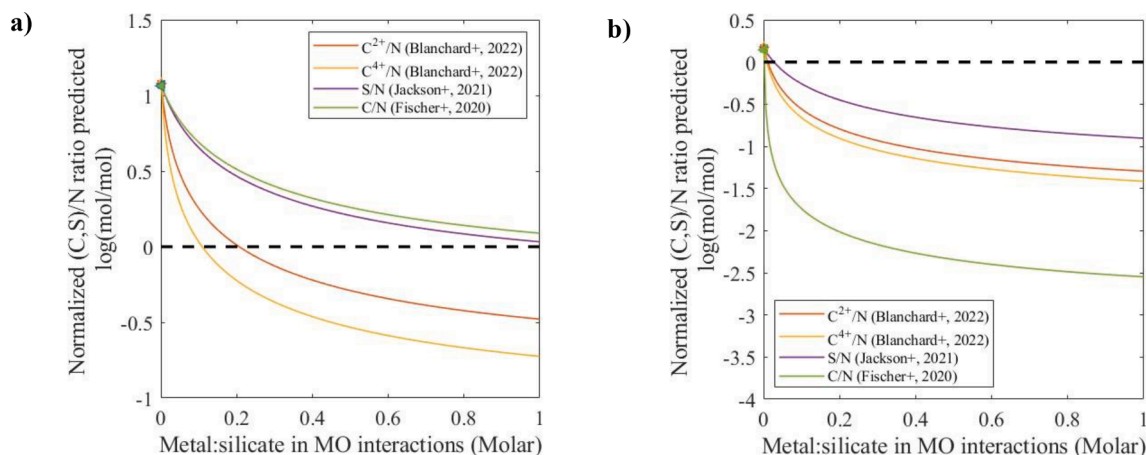


Fig. 14. (A) “reduced” impact scenario at  $\Delta IW$ -1.5, (b) “oxidized” impact scenario at  $\Delta IW$ -1.2. c/n and S/N ratios in magma ocean (MO) environments when the smaller impactor core (equilibrated at 10 GPa, 2500 K,  $\Delta IW$ -3.7 in the “reduced” and at 10 GPa, 2500 K,  $\Delta IW$ -1.7 in the “oxidized” scenario) disintegrates and interacts with the MO under extreme PT conditions (100 GPa, 5000 K). X-axis shows the extent to which the impactor core gets diluted within the MO. Y-axis shows the S/N and the C/N ratio set in the magma ocean due to the metal-silicate interactions normalized to the bulk initial elemental ratios of the first step (see main text). Ratios above solid dashed line are elevated in C/N and S/N. Symbols at zero x-axis value are impactor core elemental ratios calculated from first step (see main text).

parameter because it depends on the fluid dynamics of the dense metal falling through the magma ocean, which are still a topic of study (Dahl and Stevenson, 2010; Deguen et al., 2014; Maas et al., 2021; Qaddah et al., 2019). In this scenario, the metal/silicate ratio simply refers to the amount of silicate that the metal equilibrates with during a metal-silicate interaction. At high metal dilution (approaching 0 in Fig. 14) within the silicate mass (magma ocean), the silicate mass under equilibrium acquires the VSE chemistry of the metal it interacted with. In Fig. 14a, at high metal/silicate ratios, the predicted C/N and S/N ratios in the silicate phase are relatively low, reflecting that nitrogen is a relatively lithophile VSE near 100 GPa. Although, as metal/silicate ratios decrease (potentially reflecting more silicate entrainment in downwelling metal-rich plumes or less emulsification of the impactor core), the C/N and S/N ratios rise and approach the composition of the impactor core from the first stage calculation (Fig. 14a). Since the reduced impactor core (from first stage calculation) had highly fractionated C/N and S/N ratios, dilution of such a core within deep magma oceans can produce an elevated C/N and S/N ratio along with an additional wide range of VSE ratios depending on the amount of silicate the metal effectively interacted with.

Fig. 14b plots the predicted C/N and S/N ratios against the metal/silicate ratio associated with core backreaction within a deep magma ocean (second stage) for the “oxidized” protoplanet scenario. In this case, the impactor core from the first step calculation itself has a lower degree of VSE fractionation since nitrogen remains siderophile, although less than C and S, under low PT conditions associated with the first stage. Under deep magma ocean environments in the second step, C/N and S/N ratios in the silicate phase remain less than 1 across almost any assumed metal/silicate ratio, which is a manifestation of the oxidized impactor core having a lower C/N and S/N ratio from the first stage. As the metal/silicate ratio approaches extreme metal dilution, the C/N and S/N ratios in the silicate phase also approach the impactor core chemistry from the first stage calculation.

Fig. 15 illustrates core formation scenarios during the second stage calculation with variable metal/silicate ratios and variable VSE fractionations. Fig. 15a shows a scenario of high metal/silicate ratio under which VSE fractionations would produce low C/N and S/N ratios. In contrast, if the metal entrains a larger amount of the magma ocean that it reacts with (Fig. 15b), the magma ocean would acquire elevated C/N and S/N ratios due to the metal-silicate interaction.

Taken together, we find that backreaction of cores produced at lower

PT conditions within deep magma oceans can induce a wide variety of VSE fractionations (Fig. 15). We acknowledge that our 2-stage core formation model is rather ideal in nature and the observed C/N fractionations may be influenced by considering a) atmospheric interaction (e.g. Grewal et al., 2022a, 2021a), b) disequilibrium interaction between metal and silicate in the 2nd stage calculation (Dahl and Stevenson, 2010; Deguen et al., 2014), and c) volatile loss from the system (Gaillard et al., 2022; Kurokawa et al., 2022; Li et al., 2023; Sakuraba et al., 2021). Although, our model seeks to explore how core formation influences the chemistry of planetesimals and larger proto planets. Considering any additional processes thought to influence VSE fractionation may not change our observations as follows. Our modeling highlights the importance of redox conditions that prevailed within smaller differentiated bodies and the metal/silicate ratio associated with the backreaction of impactor cores within deeper (higher PT) magma oceans in modulating VSE ratios. Reduced bodies have a greater potential to produce cores with elevated C/N and S/N ratios compared to oxidized bodies given the partitioning of VSEs under lower PT conditions (Fig. 13). The backreaction of cores from impactors within deeper magma oceans offers a second opportunity to fractionate VSEs. Backreaction with a high associated metal/silicate ratio imparts low C/N and S/N ratios given the relative lithophile nature of N compared to other VSEs under more extreme PT conditions (Fig. 13), while backreaction with a low associated metal/silicate ratio imparts higher C/N and S/N ratios that approach the initial ratios of the impactor cores.

Our model suggests that an array of VSE ratios can be produced during metal:silicate interactions in a dynamic magma ocean – impactor core backreaction environment. If we believe in the depletion of nitrogen in present-day BSE with respect to the other VSEs (Halliday, 2013; Hirschmann, 2016; Marty, 2012), this may indicate that there was significant metal dilution within deep magma oceans during the later giant impact stages. Alternatively, if significant N is confirmed to be stored in lower mantle reservoirs, suggesting no depletion of N in BSE (e.g. Johnson and Goldblatt, 2015; Yoshioka et al., 2018), this would indicate that there may have been less effective interaction between the impactor metal and the deep magma ocean in the later giant impact stages.

## 5. Conclusion

Our study expands the PTX space where the partitioning behavior of nitrogen is constrained, particularly for extreme PT conditions and

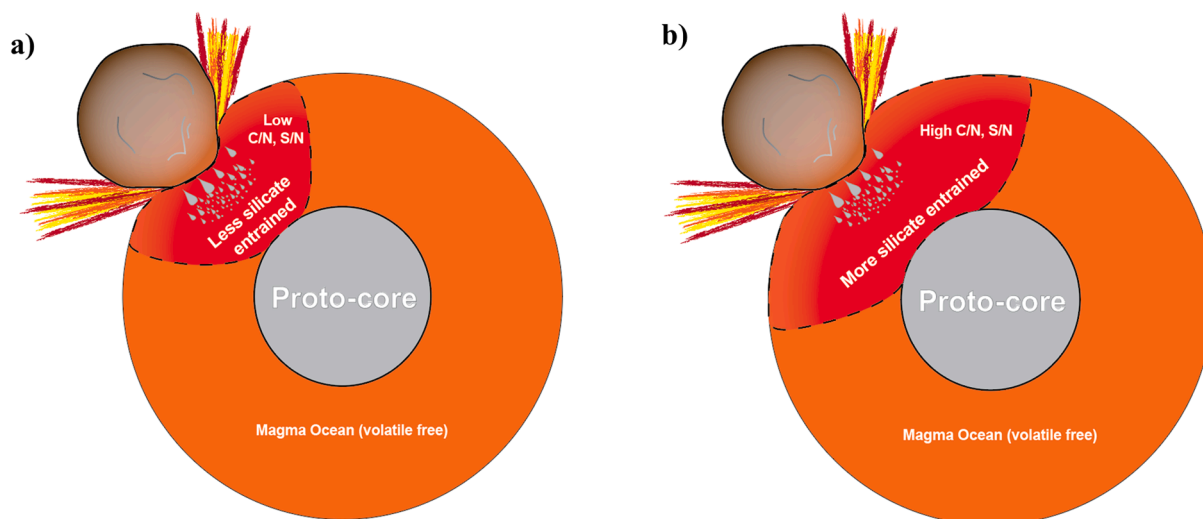


**Fig. 15.** Schematic illustrating second stage of core formation model: The impactor core (gray drops) backreacts with the portion of the magma ocean it entrains (red domains within the MO bordered by dashed lines). We model how VSEs are redistributed between metal and silicate, following their partitioning and the metal/silicate ratio of the reacting mass of impactor core and magma ocean. a) shows a lower and b) shows a higher fraction of silicate mass entrained by the downwelling core of an impactor. A greater extent of metal dilution as in b) can produce elevated C/N and S/N ratios.

depolymerized melts. We conducted laser-heated diamond anvil cell experiments and a multi-anvil experiment, spanning pressures from 15 to 103 GPa and temperatures from 2728 to 5609 K, examining silicate melts with a broad range of polymerization (NBO/T: 0.5–3.7). In addition to generating new PTX data, we compiled existing experimental data to parameterize nitrogen partitioning between metal and silicate across a wide range of PTX conditions.

Our model indicates that pressure, oxygen fugacity, and bulk nitrogen concentration of the system make nitrogen more siderophile, while temperature, oxygen and silicon content of the metallic alloy, and the SiO<sub>2</sub> content of the silicate melt makes nitrogen less siderophile.

We apply our model to explore VSE fractionations (C/N and S/N) within smaller differentiated bodies as well as in larger proto-planets due to core formation. Using a two staged core formation model, we highlight the delivery of C, S, N by cores of smaller (moon-Mars sized) “reduced” bodies as an effective way to impart elevated C/N and S/N ratios to the magma ocean of proto-Earth, during its later stages of core formation. Finally, the amount of magma ocean that the impactor core effectively interacts with during its breakdown and descent can further elevate or lower the elemental ratios.

### CRedit authorship contribution statement

**Ekanshu Mallick:** Writing – review & editing, Writing – original draft, Visualization, Validation, Software, Methodology, Investigation, Formal analysis, Data curation, Conceptualization. **Kelsey Prissel:** Writing – review & editing, Validation, Investigation. **Kevin Righter:** Writing – review & editing, Project administration. **Colin R.M. Jackson:** Writing – review & editing, Validation, Supervision, Resources, Project administration, Methodology, Investigation, Funding acquisition, Conceptualization.

### Data availability

Data are available through Mendeley data at <https://doi.org/10.17632/2r2b7p6g6m.1>.

### Declaration of competing interest

The authors declare that they have no known competing financial interests or personal relationships that could have appeared to influence the work reported in this paper.

### Acknowledgements

This project was supported by NASA Emerging Worlds Grant 80NSSC21K0377. We thank Vitali Prakapenka and Stella Chariton for support during the high-pressure experiments conducted at GeoSoilEnviroCARS (The University of Chicago, Sector 13), the Advanced Photon Source, Argonne National Laboratory, and for discussions on temperature determination using T-rax software. We thank Dongmei Cao for assistance with using the focused ion beam at Louisiana State University.

### Appendix A. Supplementary Material

Supplementary Tables S1, S2, S3, S4. Table S1 contains T-rax files which can be used to reproduce temperature estimates using the pixel ranges and wavelengths used to select ROI on light spectra captured on CCD. Table S2 and S3 contain the silicate and the metal analysis of our experiments. Table S4 contains the raw global literature data used to form Eq. 7. Table S5 contains EDS data of the starting material (glass). Supplementary pdf contains Figures S1-NBO/T vs Al<sub>2</sub>O<sub>3</sub> content of the silicate melt, S2-Multi anvil power temperature curve, S3- Comparison of pressures measured using diamond edge Raman spectroscopy with pressures measured on the heated spots using synchrotron XRD

measurements of MgO peaks, S4- Wave scans of a) nitrogen in silicate and b) nitrogen c) carbon d) oxygen in metallic alloys showing peak positions (L-value) for N, C, and O which were used to measure their concentrations, S5- shows comparison of predicted vs observed D<sub>N</sub><sup>m/s</sup> and model residual vs Si content of metal to highlight why few data points from Grewal et al. (2019a) were not included for N-parameterization, S6- correlation of raw D<sub>N</sub><sup>m/s</sup> values with PTX parameters, S7- shows the liquidus used for core formation model from Fiquet et al. (2010) and the oxygen fugacity of the “reduced” and “oxidized” scenarios used in core formation model, S8- Figure 14 (main text) recast using the Huang et al. (2024) N-model. Finally, this pdf contains a description of the 2-stage core formation model. Supplementary material to this article can be found online at <https://doi.org/10.1016/j.gca.2025.02.020>.

### References

- Agnor, C.B., Canup, R.M., Levison, H.F., 1999. On the character and consequences of large impacts in the late stage of terrestrial planet formation. *Icarus* 142, 219–237.
- Akahama, Y., Kawamura, H., 2006. Pressure calibration of diamond anvil Raman gauge to 310 GPa. *J. Appl. Phys.* 100, 043516.
- Albarède, F., 2009. Volatile accretion history of the terrestrial planets and dynamic implications.
- Alexander, C.M.O., 2022. An exploration of whether Earth can be built from chondritic components, not bulk chondrites. *Geochim. Cosmochim. Acta* 318, 428–451.
- Anders, E., Grevesse, N., 1989. Abundances of the elements: Meteoritic and solar. *Geochim. Cosmochim. Acta* 53, 197–214.
- Badro, J., Brodholt, J.P., Piet, H., Siebert, J., Ryerson, F.J., 2015. Core formation and core composition from coupled geochemical and geophysical constraints. *Proc. Natl. Acad. Sci.* 112, 12310–12314.
- Badro, J., Aubert, J., Hirose, K., Nomura, R., Blanchard, I., Borensztajn, S., Siebert, J., 2018. Magnesium Partitioning Between Earth’s Mantle and Core and its Potential to Drive an Early Exsolution Geodynamo. *Geophys. Res. Lett.* 45, 13240–13248.
- Bergin, E.A., Blake, G.A., Ciesla, F., Hirschmann, M.M., Li, J., 2015. Tracing the ingredients for a habitable earth from interstellar space through planet formation. *Proc. Natl. Acad. Sci.* 112, 8965–8970.
- Bernadou, F., Gaillard, F., Füre, E., Marrocchi, Y., Slodczyk, A., 2021. Nitrogen solubility in basaltic silicate melt - Implications for degassing processes. *Chem. Geol.* 573, 120192.
- Blanchard, I., Rubie, D.C., Jennings, E.S., Franchi, I.A., Zhao, X., Petitgirard, S., Miyajima, N., Jacobson, S.A., Morbidelli, A., 2022. The metal-silicate partitioning of carbon during Earth’s accretion and its distribution in the early solar system. *Earth Planet. Sci. Lett.* 580, 117374.
- Braukmüller, N., Wombacher, F., Funk, C., Münker, C., 2019. Earth’s volatile element depletion pattern inherited from a carbonaceous chondrite-like source. *Nat. Geosci.* 12, 564–568.
- Campbell, A.J., Danielson, L., Righter, K., Seagle, C.T., Wang, Y., Prakapenka, V.B., 2009. High pressure effects on the iron-iron oxide and nickel-nickel oxide oxygen fugacity buffers. *Earth Planet. Sci. Lett.* 286, 556–564.
- Canup, R.M., Asphaug, E., 2001. Origin of the Moon in a giant impact near the end of the Earth’s formation. *Nature* 412, 708–712.
- Dahl, T.W., Stevenson, D.J., 2010. Turbulent mixing of metal and silicate during planet accretion — And interpretation of the Hf-W chronometer. *Earth Planet. Sci. Lett.* 295, 177–186.
- Dalou, C., Hirschmann, M.M., von der Handt, A., Mosenfelder, J., Armstrong, L.S., 2017. Nitrogen and carbon fractionation during core-mantle differentiation at shallow depth. *Earth Planet. Sci. Lett.* 458, 141–151.
- Dalou, C., Füre, E., Deligny, C., Piani, L., Caumon, M.-C., Laumonier, M., Boulliang, J., Edén, M., 2019a. Redox control on nitrogen isotope fractionation during planetary core formation. *Proc. Natl. Acad. Sci. U.S.A.* 116, 14485–14494.
- Dalou, C., Hirschmann, M.M., Jacobsen, S.D., Le Losq, C., 2019b. Raman spectroscopy study of C-O-H-N speciation in reduced basaltic glasses: Implications for reduced planetary mantles. *Geochim. Cosmochim. Acta* 265, 32–47.
- Dasgupta, R., Falken, E., Pal, A., Sun, C., 2022. The fate of nitrogen during parent body partial melting and accretion of the inner solar system bodies at reducing conditions. *Geochim. Cosmochim. Acta* 336, 291–307.
- Davies, G.F., 1985. Heat deposition and retention in a solid planet growing by impacts. *Icarus* 63, 45–68.
- Deguen, R., Landeau, M., Olson, P., 2014. Turbulent metal-silicate mixing, fragmentation, and equilibration in magma oceans. *Earth Planet. Sci. Lett.* 391, 274–287.
- Dobrosavljevic, V.V., Zhang, D., Sturhahn, W., Chariton, S., Prakapenka, V.B., Zhao, J., Toellner, T.S., Pardo, O.S., Jackson, J.M., 2023. Melting and defect transitions in FeO up to pressures of Earth’s core-mantle boundary. *Nat Commun* 14, 7336.
- Elkins-Tanton, L.T., 2012. Magma Oceans in the Inner Solar System. *Annu. Rev. Earth Planet. Sci.* 40, 113–139.
- Fiquet, G., Auzende, A.L., Siebert, J., Corgne, A., Bureau, H., Ozawa, H., Garbarino, G., 2010. Melting of Peridotite to 140 Gigapascals. *Science* 329, 1516–1518.
- Fischer, R.A., Nakajima, Y., Campbell, A.J., Frost, D.J., Harries, D., Langenhorst, F., Miyajima, N., Pollok, K., Rubie, D.C., 2015. High pressure metal-silicate partitioning of Ni, Co, V, Cr, Si, and O. *Geochim. Cosmochim. Acta* 167, 177–194.



- Fischer, R.A., Cottrell, E., Hauri, E., Lee, K.K.M., Le Voyer, M., 2020. The carbon content of Earth and its core. *Proc. Natl. Acad. Sci.* 117, 8743–8749.
- Fudali, R.F., 1965. Oxygen fugacities of basaltic and andesitic magmas. *Geochim. Cosmochim. Acta* 29, 1063–1075.
- Gaillard, F., Bernadou, F., Roskosz, M., Bouhifd, M.A., Marrocchi, Y., Iacono-Marziano, G., Moreira, M., Scaillet, B., Rogerie, G., 2022. Redox controls during magma ocean degassing. *Earth Planet. Sci. Lett.* 577, 117255.
- Genda, H., Abe, Y., 2003. Modification of a proto-lunar disk by hydrodynamic escape of silicate vapor. *Earth Planet. Sci. Lett.* 55, 53–57.
- Ghiorso, M.S., Carmichael, I.S.E., 1980. A regular solution model for met-aluminous silicate liquids: Applications to geothermometry, immiscibility, and the source regions of basic magmas. *Contrib. Mineral. and Petrol.* 71, 323–342.
- Green, D.H., Ringwood, A.E., 1963. Mineral assemblages in a model mantle composition. *J. Geophys. Res.* 1896–1977 (68), 937–945.
- Grewal, D.S., Dasgupta, R., Holmes, A.K., Costin, G., Li, Y., Tsuno, K., 2019a. The fate of nitrogen during core-mantle separation on Earth. *Geochim. Cosmochim. Acta* 251, 87–115.
- Grewal, D.S., Dasgupta, R., Sun, C., Tsuno, K., Costin, G., 2019b. Delivery of carbon, nitrogen, and sulfur to the silicate Earth by a giant impact. *Sci. Adv.* 5, eaau3669.
- Grewal, D.S., Dasgupta, R., Farnell, A., 2020. The speciation of carbon, nitrogen, and water in magma oceans and its effect on volatile partitioning between major reservoirs of the Solar System rocky bodies. *Geochim. Cosmochim. Acta* 280, 281–301.
- Grewal, D.S., Dasgupta, R., Hough, T., Farnell, A., 2021a. Rates of protoplanetary accretion and differentiation set nitrogen budget of rocky planets. *Nat. Geosci.* 14, 369–376.
- Grewal, D.S., Dasgupta, R., Marty, B., 2021b. A very early origin of isotopically distinct nitrogen in inner Solar System protoplanets. *Nat. Astron.* 5, 356–364.
- Grewal, D.S., Seales, J.D., Dasgupta, R., 2022a. Internal or external magma oceans in the earliest protoplanets – Perspectives from nitrogen and carbon fractionation. *Earth Planet. Sci. Lett.* 598, 117847.
- Grewal, D.S., Sun, T., Aithala, S., Hough, T., Dasgupta, R., Yeung, L.Y., Schauble, E.A., 2022b. Limited nitrogen isotopic fractionation during core-mantle differentiation in rocky protoplanets and planets. *Geochim. Cosmochim. Acta* 338, 347–364.
- Grewal, D.S., Miyazaki, Y., Nie, N.X., 2024. Contribution of the Moon-forming Impactor to the Volatile Inventory in the Bulk Silicate Earth. *Planet. Sci. J.* 5, 181.
- Häglund, J., Fernández Guillermot, A., Grimvall, G., Körling, M., 1993. Theory of bonding in transition-metal carbides and nitrides. *Phys. Rev. B* 48, 11685–11691.
- Halliday, A.N., 2013. The origins of volatiles in the terrestrial planets. *Geochim. Cosmochim. Acta* 105, 146–171.
- Halliday, A.N., Wänke, H., Birk, J.-L., Clayton, R.N., 2001. The Accretion, Composition and Early Differentiation of Mars. *Space Sci. Rev.* 96, 197–230.
- Hellmann, J.L., Hopp, T., Burkhardt, C., Kleine, T., 2020. Origin of volatile element depletion among carbonaceous chondrites. *Earth Planet. Sci. Lett.* 549, 116508.
- Hirschmann, M.M., 2016. Constraints on the early delivery and fractionation of Earth's major volatiles from C/H, C/N, and C/S ratios. *Am. Mineral.* 101, 540–553.
- Hirschmann, M.M., Baker, M.B., Stolper, E.M., 1998. The Effect of Alkalies on the Silica Content of Magma-Derived Melts. *Geochim. Cosmochim. Acta* 62, 883–902.
- Hirschmann, M.M., Bergin, E.A., Blake, G.A., Ciesla, F.J., Li, J., 2021. Early volatile depletion on planetesimals inferred from C–S systematics of iron meteorite parent bodies. *Proc. Natl. Acad. Sci.* 118, e2026779118.
- Holzheid, A., Sylvester, P., O'Neill, H.S.C., Rubie, D.C., Palme, H., 2000. Evidence for a late chondritic veneer in the Earth's mantle from high-pressure partitioning of palladium and platinum. *Nature* 406, 396–399.
- Huang, D., Badro, J., Brodholt, J., Li, Y., 2019. Ab Initio Molecular Dynamics Investigation of Molten Fe–Si–O in Earth's Core. *Geophys. Res. Lett.* 46, 6397–6405.
- Huang, D., Brodholt, J., Sossi, P., Li, Y., Murakami, M., 2022a. Nitrogen Speciation in Silicate Melts at Mantle Conditions From Ab Initio Simulations. *Geophys. Res. Lett.* 49, e2021GL095546.
- Huang, D., Murakami, M., Brodholt, J., McCammon, C., Petitgirard, S., 2022b. Structural evolution in a pyrolytic magma ocean under mantle conditions. *Earth Planet. Sci. Lett.* 584, 117473.
- Huang, D., Siebert, J., Sossi, P., Kubik, E., Avicé, G., Murakami, M., 2024. Nitrogen sequestration in the core at megabar pressure and implications for terrestrial accretion. *Geochim. Cosmochim. Acta*.
- Jackson, C.R.M., Bennett, N.R., Du, Z., Cottrell, E., Fei, Y., 2018. Early episodes of high-pressure core formation preserved in plume mantle. *Nature* 553, 491–495.
- Jackson, C.R.M., Cottrell, E., Du, Z., Bennett, N.R., Fei, Y., 2021. High pressure redistribution of nitrogen and sulfur during planetary stratification. *Geochim. Persp. Lett.* 37–42.
- Johnson, B., Goldblatt, C., 2015. The nitrogen budget of Earth. *Earth Sci. Rev.* 148, 150–173.
- Kadik, A.A., Kurovskaya, N.A., Ignat'ev, Yu.A., Kononkova, N.N., Koltashev, V.V., Plotnichenko, V.G., 2011. Influence of oxygen fugacity on the solubility of nitrogen, carbon, and hydrogen in FeO–Na<sub>2</sub>O–SiO<sub>2</sub>–Al<sub>2</sub>O<sub>3</sub> melts in equilibrium with metallic iron at 1.5 GPa and 1400°C. *Geochim. Int.* 49, 429–438.
- Kadik, A.A., Litvin, Y.A., Koltashev, V.V., Kryukova, E.B., Plotnichenko, V.G., Tsekhnova, T.I., Kononkova, N.N., 2013. Solution behavior of reduced N–H–O volatiles in FeO–Na<sub>2</sub>O–SiO<sub>2</sub>–Al<sub>2</sub>O<sub>3</sub> melt equilibrated with molten Fe alloy at high pressure and temperature. *Phys. Earth Planet. In.* 214, 14–24.
- Karki, B.B., Bhattarai, D., Mookherjee, M., Stixrude, L., 2010. Visualization-based analysis of structural and dynamical properties of simulated hydrous silicate melt. *Phys. Chem. Minerals* 37, 103–117.
- Kurokawa, H., Laneuville, M., Li, Y., Zhang, N., Fujii, Y., Sakuraba, H., Houser, C., Cleaves II, H.J., 2022. The Origin of Earth's Mantle Nitrogen: Primordial or Early Biogeochemical Cycling? *Geochim. Geophys. Geosyst.* 23, e2021GC010295.
- Lammer, H., Kasting, J.F., Chassefière, E., Johnson, R.E., Kulikov, Y.N., Tian, F., 2008. Atmospheric escape and evolution of terrestrial planets and satellites. *Space Sci. Rev.* 139, 399–436.
- LaTourrette, T., Wasserburg, G.J., 1998. Mg diffusion in anorthite: implications for the formation of early solar system planetesimals. *Earth Planet. Sci. Lett.* 158, 91–108.
- Lee, T., Papanastassiou, D.A., Wasserburg, G.J., 1976. Correction [to “Demonstration of 26Mg excess in Allende and evidence for 26Al”]. *Geophys. Res. Lett.* 3, 109–112.
- Li, Y.-F., Marty, B., Shcheka, S., Zimmermann, L., Keppler, H., 2016. Nitrogen isotope fractionation during terrestrial core-mantle separation. *Geochim. Perspect. Lett.* 2, 138–147.
- Li, Y., Wiedenbeck, M., Monteleone, B., Dasgupta, R., Costin, G., Gao, Z., Lu, W., 2023. Nitrogen and carbon fractionation in planetary magma oceans and origin of the superchondritic C/N ratio in the bulk silicate Earth. *Earth Planet. Sci. Lett.* 605, 118032.
- Libourel, G., Marty, B., Humbert, F., 2003. Nitrogen solubility in basaltic melt. Part I. Effect of oxygen fugacity. *Geochim. Cosmochim. Acta* 67, 4123–4135.
- Lodders, K., 2003. Solar System Abundances and Condensation Temperatures of the Elements. *ApJ* 591, 1220–1247.
- Ma, Z., 2001. Thermodynamic description for concentrated metallic solutions using interaction parameters. *Metal Mater Trans B* 32, 87–103.
- Maas, C., Manske, L., Wünnemann, K., Hansen, U., 2021. On the fate of impact-delivered metal in a terrestrial magma ocean. *Earth Planet. Sci. Lett.* 554, 116680.
- Mao, H.K., Bell, P.M., Shaner, J.W., Steinberg, D.J., 2008. Specific volume measurements of Cu, Mo, Pd, and Ag and calibration of the ruby R1 fluorescence pressure gauge from 0.06 to 1 Mbar. *J. Appl. Phys.* 49, 3276–3283.
- Marty, B., 2012. The origins and concentrations of water, carbon, nitrogen and noble gases on Earth. *Earth Planet. Sci. Lett.* 313–314, 56–66.
- Marty, B., Almayrac, M., Barry, P.H., Bekaert, D.V., Broadley, M.W., Byrne, D.J., Ballentine, C.J., Caracausi, A., 2020. An evaluation of the C/N ratio of the mantle from natural CO<sub>2</sub>-rich gas analysis: Geochemical and cosmochemical implications. *Earth Planet. Sci. Lett.* 551, 116574.
- Mosenfelder, J.L., Von Der Handt, A., Füre, E., Dalou, C., Hervig, R.L., Rossman, G.R., Hirschmann, M.M., 2019. Nitrogen incorporation in silicates and metals: Results from SIMS, EPMA, FTIR, and laser-extraction mass spectrometry. *Am. Mineral.* 104, 31–46.
- Moynier, F., Day, J.M.D., Okui, W., Yokoyama, T., Bouvier, R.J., Podosek, F.A., 2012. Planetary-scale strontium isotopic heterogeneity and the age of volatile depletion of early Solar System materials. *ApJ* 758, 45.
- Mysen, B.O., Tomita, T., Ohtani, E., Suzuki, A., 2014. Speciation of D/H partitioning between fluids and melts in silicate-D-O-H-C-N systems determined in-situ at upper mantle temperatures, pressures, and redox conditions. *Am. Mineral.* 99, 578–588.
- Newcombe, M.E., Nielsen, S.G., Peterson, L.D., Wang, J., Alexander, C.M.O., Sarafian, A.R., Shimizu, K., Nittler, L.R., Irving, A.J., 2023. Degassing of early-formed planetesimals restricted water delivery to Earth. *Nature* 615, 854–857.
- O'Neill, H., St, C., Eggins, S.M., 2002. The effect of melt composition on trace element partitioning: an experimental investigation of the activity coefficients of FeO, NiO, CoO, MoO<sub>2</sub> and MoO<sub>3</sub> in silicate melts. *Chem. Geol.* 186, 151–181.
- O'Neill, H.S.C., 1987. Quartz-fayalite-iron and quartz-fayalite-magnetite equilibria and the free energy of formation of fayalite (Fe<sub>2</sub>SiO<sub>4</sub>) and magnetite (Fe<sub>3</sub>O<sub>4</sub>). *American Mineralogist* 72, 67–75.
- Ono, S., Kikagawa, T., Hirao, N., Mibe, K., 2010. Letter. High-pressure magnetic transition in hcp-Fe. *Am. Mineral.* 95, 880–883.
- Palme, H., Lodders, K., Jones, A., 2014. Solar System Abundances of the Elements. Planets, Asteroids, Comets and the Solar System, Volume 2 of Treatise on Geochemistry (Second Edition). Edited by Andrew M. Davis. Elsevier, 2014., p.15–36 2.
- Prescher, C., Prakapenka, V.B., 2015. DIOPTAS: a program for reduction of two-dimensional X-ray diffraction data and data exploration. *High Pressure Res.* 35, 223–230.
- Qaddah, B., Monteux, J., Clesi, V., Bouhifd, M.A., Le Bars, M., 2019. Dynamics and stability of an iron drop falling in a magma ocean. *Phys. Earth Planet. In.* 289, 75–89.
- Righter, K., Rowland II, R., Yang, S., Humayun, M., 2020. Activity coefficients of siderophile elements in Fe-Si liquids at high pressure. *Geochim. Persp. Lett.* 44–49.
- Roskosz, M., Bouhifd, M.A., Jephcoat, A.P., Marty, B., Mysen, B.O., 2013. Nitrogen solubility in molten metal and silicate at high pressure and temperature. *Geochim. Cosmochim. Acta* 121, 15–28.
- Rubie, D.C., Frost, D.J., Mann, U., Asahara, Y., Nimmo, F., Tsuno, K., Kegler, P., Holzheid, A., Palme, H., 2011. Heterogeneous accretion, composition and core-mantle differentiation of the Earth. *Earth Planet. Sci. Lett.* 301, 31–42.
- Sakuraba, H., Kurokawa, H., Genda, H., Ohta, K., 2021. Numerous chondritic impactors and oxidized magma ocean set Earth's volatile depletion. *Sci. Rep.* 11, 20894.
- Schlichting, H.E., Sari, R., Yalinewich, A., 2015. Atmospheric mass loss during planet formation: The importance of planetesimal impacts. *Icarus* 247, 81–94.
- Sekiya, M., Nakazawa, K., Hayashi, C., 1980. Dissipation of the Primordial Terrestrial Atmosphere Due to Irradiation of the Solar EUV. *Prog. Theor. Phys.* 64, 1968–1985.
- Sha, X., Cohen, R.E., 2010. First-principles thermal equation of state and thermoelasticity of hcp Fe at high pressures. *Phys. Rev. B* 81, 094105.
- Shen, G., Wang, Y., Dewaele, A., Wu, C., Frantanduono, D.E., Eggert, J., Klotz, S., Dziubek, K.F., Loubeyre, P., Fat'yanov, O.V., Asimow, P.D., Mashimo, T., Wentzcovitch, R.M. M., 2020. Toward an international practical pressure scale: A proposal for an IPPS ruby gauge (IPPS-Ruby2020). *High Pressure Research* 40, 299–314.
- Shi, L., Lu, W., Kagoshima, T., Sano, Y., Gao, Z., Du, Z., Liu, Y., Fei, Y., Li, Y., 2022. Nitrogen isotope evidence for Earth's heterogeneous accretion of volatiles. *Nat Commun* 13, 4769.
- Siebert, J., Badro, J., Antonangeli, D., Ryerson, F.J., 2012. Metal-silicate partitioning of Ni and Co in a deep magma ocean. *Earth Planet. Sci. Lett.* 321–322, 189–197.



- Speelmanns, I.M., Schmidt, M.W., Liebske, C., 2019. The almost lithophile character of nitrogen during core formation. *Earth Planet. Sci. Lett.* 510, 186–197.
- Suer, T.-A., Jackson, C., Grewal, D.S., Dalou, C., Lichtenberg, T., 2023. The distribution of volatile elements during rocky planet formation. *Front. Earth Sci.* 11.
- Tagawa, S., Sakamoto, N., Hirose, K., Yokoo, S., Hernlund, J., Ohishi, Y., Yurimoto, H., 2021. Experimental evidence for hydrogen incorporation into Earth's core. *Nat Commun* 12, 2588.
- Tonks, W.B., Melosh, H.J., 1993. Magma ocean formation due to giant impacts. *J. Geophys. Res. Planets* 98, 5319–5333.
- Tucker, J.M., Mukhopadhyay, S., 2014. Evidence for multiple magma ocean outgassing and atmospheric loss episodes from mantle noble gases. *Earth Planet. Sci. Lett.* 393, 254–265.
- Urey, H.C., 1956. The cosmic abundances of potassium, uranium, and thorium and the heat balances of the Earth, the Moon, and Mars. *Proc. Natl. Acad. Sci.* 42 (12), 889–891.
- Vollstaedt, H., Mezger, K., Alibert, Y., 2020. Carbonaceous Chondrites and the Condensation of Elements from the Solar Nebula. *ApJ* 897, 82.
- Wang, Z., Becker, H., 2013. Ratios of S, Se and Te in the silicate Earth require a volatile-rich late veneer. *Nature* 499, 328–331.
- Wasson, J.T., Kallemeyn, G.W., Runcorn, S.K., Turner, G., Woolfson, M.M., 1997. Compositions of chondrites. *Philosophical Transactions of the Royal Society of London. Series a, Mathematical and Physical Sciences* 325, 535–544.
- Wetherill, G.W., 1980. Formation of the Terrestrial Planets. *Ann. Rev. Astron. Astrophys.* 18, 77–113.
- Wetherill, G.W., 1985. Occurrence of Giant Impacts during the Growth of the Terrestrial Planets. *Science* 228, 877–879.
- Wu, Z., Wentzcovitch, R.M., Umemoto, K., Li, B., Hirose, K., Zheng, J.-C., 2008. Pressure-volume-temperature relations in MgO: An ultrahigh pressure-temperature scale for planetary sciences applications. *J. Geophys. Res. Solid Earth* 113.
- Yoshioka, T., Wiedenbeck, M., Shcheka, S., Keppler, H., 2018. Nitrogen solubility in the deep mantle and the origin of Earth's primordial nitrogen budget. *Earth Planet. Sci. Lett.* 488, 134–143.